Integration of mouse ovary morphogenesis with developmental dynamics of the oviduct, ovarian ligaments, and rete ovarii.

Jennifer McKey[1], Dilara N. Anbarci[1], Corey Bunce[1], Alejandra E. Ontiveros[2], Richard R. Behringer[2], and Blanche Capel[1]*

[1]*Department of Cell Biology, Duke University Medical Center, Durham NC 27710*

[2]*Department of Genetics, University of Texas MD Anderson Cancer Center, Houston, TX, 77030*

*Corresponding author: blanche.capel@duke.edu

Keywords: ovary; morphogenesis; oviduct; rete ovarii; gonad; lightsheet; cranial suspensory ligament

Abstract

Morphogenetic events during development of the fetal ovary are crucial to the establishment of female fertility. However, the effects of structural rearrangements of the ovary and surrounding reproductive tissues on ovary morphogenesis remain largely uncharacterized. Using tissue clearing and lightsheet microscopy, we found that ovary folding correlated with regionalization into cortex and medulla. Relocation of the oviduct to the ventral aspect of the ovary led to ovary encapsulation, and mutual attachment of the ovary and oviduct to the cranial suspensory ligament likely triggered ovary folding. Development of the rete ovarii correlated with events of ovary morphogenesis. Using genetic mouse models in which the oviduct and rete ovarii are perturbed, we found the oviduct is required for ovary encapsulation. This study reveals novel relationships among the ovary and surrounding tissues and paves the way for functional investigation of the relationship between architecture and differentiation of the mammalian ovary.

Introduction

During mouse fetal development, the gonad first arises on the ventromedial aspect of the mesonephros (Brambell and Hill, 1927; Harikae et al., 2013; Karl and Capel, 1998; Windley and Wilhelm, 2015). In XX embryos, the gonads develop into ovaries, where supporting cells become granulosa cells, interstitial cells become theca cells and other stromal cell types, and germ cells become oocytes (Nef et al., 2019; Rastetter et al., 2014; Stévant et al., 2019; Wilhelm et al., 2013). As these cells undergo differentiation between E11.5 and birth, they progressively assemble into individual ovarian follicles, characterized by the presence of one oocyte surrounded by two or three pre-granulosa cells (Lei and Spradling, 2016, 2013; Liu et al., 2010; Mork et al., 2012; Pepling and Lei, 2018; Pepling, 2012; Zheng et al., 2014).The advent of single cell transcriptomics has provided a wealth of information on the cellular profiles and gene expression trajectories within the developing ovary, presenting an unprecedented view of the molecular and cellular pathways at play during mammalian ovary differentiation and follicle formation (Li et al., 2017; Liu et al., 2010; Mayère et al., 2021; Niu and Spradling, 2020; Stévant et al., 2019). However, transcriptomics alone do not address the spatial and structural components that underlie ovary regionalization and patterning. In fact, while granulosa cells and oocytes are locally assembling into follicles, the ovary as a whole undergoes dramatic changes in shape and cell composition, including the integration of extrinsic components such as lymphatics, mesenchymal theca cells, and innervation (Liu et al., 2015; McKey et al., 2019; Svingen et al., 2012). The events that occur during ovary morphogenesis are poorly defined and lack context, owing in part to the scarcity of molecular and imaging tools to study the ovary in detail. In addition, tissues closely associated with the ovary, such as the Müllerian duct (MD), ovarian ligaments and the rete ovarii, that also undergo dramatic transitions during development (Adham et al., 2002; Ford et al., 2020; Lee et al., 2011; Wenzel and Odend'hal, 1985) have been studied individually, but not in the context of ovary morphogenesis. Consequently, their impact on ovary morphogenesis has been overlooked. With recent advances in tissue clearing and 3D imaging technology, it is now possible to visualize structural changes at the level of the whole gonad or even the whole embryo (Bunce et al., 2021; Fiorentino et al., 2021; Soygur et al., 2021a; Soygur et al.; 2021b). We recently developed a tissue-clearing method that combines CUBIC and iDISCO (McKey et al., 2020; Renier et al., 2014; Susaki et al., 2015), and optimized 3D imaging methods using lightsheet microscopy to visualize the fetal and perinatal ovary *in situ*, in the context of its surrounding tissues (McKey et al., 2019).

Using our 3D-imaging methods and high-resolution confocal microscopy, we provide a detailed and contextual description of mouse ovary morphogenesis from E14.5 to birth. We define three discrete hallmarks of ovary morphogenesis: (1) ovary folding, (2) specification of medullary and cortical compartments, and (3) ovary encapsulation. We integrated this morphometric approach with a detailed study of three tissues closely associated with the ovary: the ovarian ligaments, the Müllerian duct and the rete ovarii, and found compelling correlations between the developmental dynamics of these tissues and ovary morphogenesis. Finally, we found that different combinations of *Pax2* and *Pax8* deletion alleles

perturb the oviduct and/or regions of the rete ovarii differentially, and lead to disruptions in ovary morphogenesis.

Results

3D models of developing ovaries provide a new perspective on ovary morphology.

The gonad first arises on the coelomic surface of the mesonephros. Early gonads are generally visualized and studied in complex with the mesonephros, which hosts the developing reproductive ducts. The mesonephric duct, which gives rise to the Wolffian duct (WD), is present from the onset of gonadogenesis (Brambell, 1927; Kobayashi and Behringer, 2003; Zhao and Yao, 2019). However, the Müllerian duct develops later by invagination of the mesonephric epithelium between E11.5 to E13.5 in the mouse (Huang et al., 2014; Mullen and Behringer, 2014; Orvis and Behringer, 2007; Roly et al., 2018). While both Wolffian and Müllerian ducts initially develop in all embryos, only one is maintained depending on the sex of the embryo. In female embryos, the Wolffian duct fully regresses by E15.5 (Zhao et al., 2021), while the Müllerian duct is maintained and gives rise to the oviduct (most proximate to the ovary), the uterus, the cervix and the anterior aspect of the vagina (Kobayashi and Behringer, 2003).

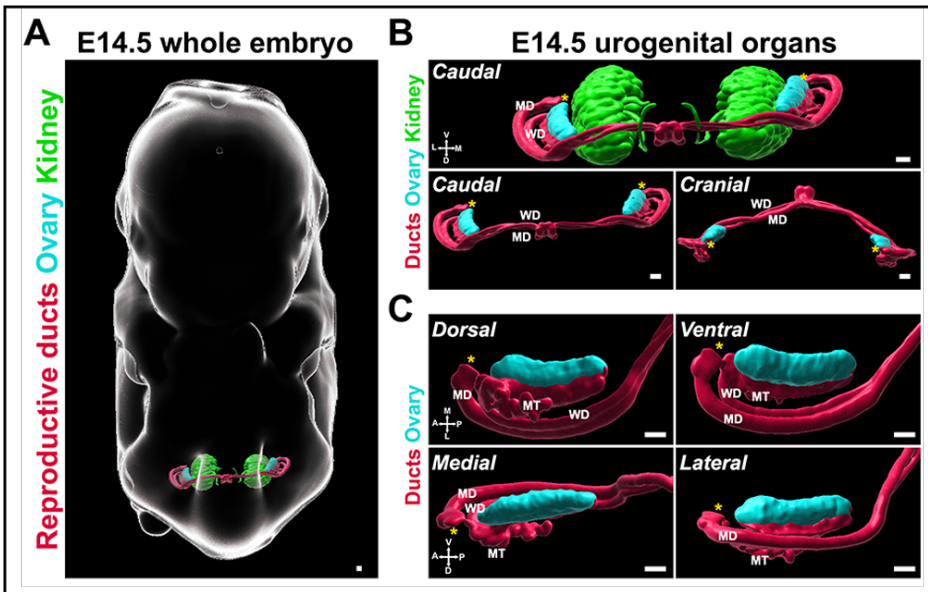

Figure 1. 3D models of developing ovaries provide a new perspective of ovary morphology. (**A**) 3D model generated by isosurface segmentation of lightsheet images taken of a whole XX embryo at E14.5 immunostained for PAX8 (kidney, *green;* reproductive ducts, *red*) and FOXL2 (gonad, *cyan*). (**B**) Caudal and cranial views of the surfaces representing the urogenital system, with and without the kidney surfaces, isolated from the whole embryo images in **A**. (**C**) Close-ups of dorsal, ventral, medial and lateral views of the surfaces representing the ovary and reproductive ducts, isolated from the images in **A**. MD, Müllerian duct; WD, Wolffian duct; MT, mesonephric tubules. Yellow asterisks indicate the location of the infundibulum of the presumptive oviduct for reference. Compasses on the bottom left of each panel indicate the orientation of the ovary: V, ventral; L, lateral; D, dorsal; M, medial; A, anterior; P, posterior. Scale bars, 100μm.

We chose E14.5 as the starting stage for our study, as this precedes the major changes in shape and conformation that are specific to the female gonad. To determine the optimal angles to assess ovary morphology, we first performed immunostaining of whole XX embryos at E14.5 with antibodies against FOXL2, which is expressed in pre-granulosa cells and serves as a marker of the gonadal domain, and antibodies against PAX8, which is expressed in the epithelium of the reproductive ducts and cells of the developing kidney. These samples were cleared using iDISCO and imaged with lightsheet microscopy

(Bunce et al., 2021; Renier et al., 2014). We generated 3D models of the labelled structures using isosurface segmentation to provide a morphological view of the urogenital complex *in situ* (Fig. 1A, Fig. S1A, Movie S1). We found that at E14.5 the bilateral gonad/mesonephros complexes resided in the posterior third of the embryo, in a plane orthogonal to the midline axis of the embryo (Fig. 1A) located on the ventro-lateral aspect of the developing kidneys (Fig. 1B). A recent study combining contextual 3D images of the developing gonads in the whole embryo with quantitative morphometric analysis showed that the entire genital ridge rotates inward from E10.5 to E12.5 (Bunce et al., 2021), thus by E12.5 the gonads appear on the medial aspect of the mesonephros. Consistent with these observations, at E14.5 the reproductive ducts were located lateral to the gonads, which were oriented towards each other in the medial axis (Fig. 1B). We used the 3D objects representing the ovaries and ducts in this image to define the six views that are presented throughout this study (Fig. 1C). The caudal and cranial views best illustrated the position and shifts of the ducts relative to the ovary (Fig. 1B), while the dorsal, medial, lateral and ventral views provided information on the shape and regionalization of the ovary itself (Fig. 1C). Dorsal and ventral views also provided context on the position and development of the individual ducts and mesonephric tubules inside the mesonephros (Fig. 1C, *top panels*). Lateral and medial views were optimal for observing the dorsal/ventral regionalization of the ovary and the interface between the gonad and the mesonephros (Fig. 1C, *bottom panels*).

The ovary transitions from elongated to crescent-shaped during late gestation.

Having defined the contextual components of ovary development at E14.5 and the optimal ways of visualizing morphogenetic changes, we next studied the shape of the ovary from E14.5 to birth. For this, we used immunostaining with antibodies against FOXL2 and first imaged whole-mount gonad/mesonephros complexes using confocal microscopy (Fig. 2A). At E14.5, the ovary was still shaped as an elongated tissue developing on the medial face of the mesonephros. By E17.5, the ovary adopted a rounder conformation. The dorsal side eventually resembled a crescent shape in E18.5 embryos (Fig. 2A). This change in conformation was accompanied by a hollowing of the FOXL2 domain in the center of the dorsal face of the ovary (Fig. 2A). We next investigated the dynamics of the FOXL2+ domain in whole ovaries cleared with iDISCO+CUBIC and imaged with lightsheet microscopy (Fig. S1A, B; Movie S2). The advantage of this method is that the sample was imaged in its native conformation, in a cylinder of agarose, and thus did not undergo artificial deformation resulting from mounting on a slide (Fig. S1A, B). With these 3D models, we better visualized the conformation of the ovary in space, and observed a similar shift from an elongated to a crescent shape between E14.5 and birth (postnatal day 0, P0) (Fig. 2B). This was most visible on the dorsal and ventral sides of the ovary, where anterior and posterior regions appeared to rise toward the medial axis and come closer to each other. This was associated with an increase in the inflexion towards the center of the ovary, and with an ingression of the medial face of the ovary, leading to an increase in the concavity of the lateral face (Fig. 2B). Our data thus suggest that the change in conformation of the ovary is representative of a folding process resulting in the center inflexion of the ovary and relocation of anterior and posterior poles.

Upon closer observation, we found that the anterior portion of the ovary appeared to thicken and shift up above the middle of the ovary, suggesting that the anterior region is subject to more deformation than the posterior region (Fig. 2B). Caudal and cranial views of the process showed that while the ventral surface of the ovary remained smooth during ovary folding, a lateral protrusion extended from the mid-region of the dorsal face between E14.5 and E17.5 (Fig. 2C, *white arrows*).

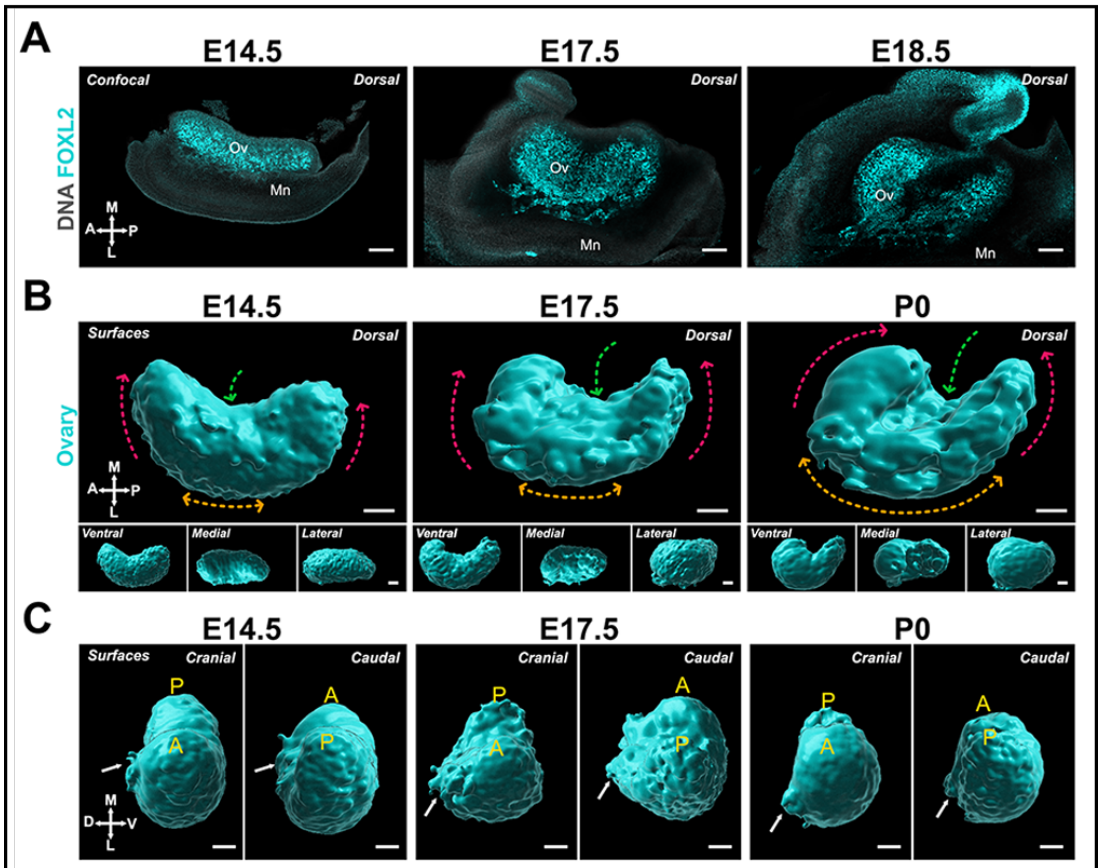

Figure 2. The ovary transitions from elongated to crescent-shaped during late gestation. (**A**) Optical sections from confocal Z-stacks of whole immunostaining of ovary/mesonephros complexes at E14.5, E17.5 and E18.5 immunostained for FOXL2 (*cyan*) and counterstained with Hoechst nuclear dye (*grayscale*). (**B**) 3D model generated by isosurface segmentation of lightsheet images taken of whole ovaries at E14.5, E17.5 and P0 immunostained for FOXL2 (*cyan*). Top large panels represent the dorsal view, while small bottom panels illustrate ventral, medial and lateral views of the same ovary. Dashed arrows illustrate the change in conformation of the ovary as it develops: red arrows, relocation of the anterior and posterior poles; green arrows, medial inflexion; orange arrows, increase in lateral concavity. (**C**) Cranial and caudal views of the surface of the ovaries presented in **B**. White arrows point to the dorsal protrusion of the ovarian domain. A, anterior pole; P, posterior pole. Ov, ovary; Mn, mesonephros; MD, Müllerian duct. Compasses on the bottom left of each panel indicate the orientation of the ovary: V, ventral; L, lateral; D, dorsal; M, medial; A, anterior; P, posterior. Scale bars, 100μm.

Ovary folding results in specification of the medullary and cortical compartments of the ovary.

Previous studies have shown that the location of individual follicles inside the ovary carries functional significance (Cordeiro et al., 2015; Mork et al., 2012; Suzuki et al., 2015, Zheng et al. 2014). Although follicles assembled during late gestation in the medullary compartment of the ovary initiate growth shortly after birth, they become atretic during the juvenile period and are all depleted by the onset of puberty. In parallel, a new wave of *de novo* follicle formation occurs around birth in the cortical compartment (Mork et al., 2012; Niu and Spradling, 2020; Zheng et al., 2014). These constitute the finite pool of ovarian follicles that remain quiescent throughout the juvenile period and begin to sequentially activate and initiate growth cyclically at the onset of puberty and until menopause, thus supporting the entire female reproductive lifespan (Duncan and Gerton, 2018; Mork et al., 2012; Zheng et al., 2014). While this functional regionalization points to the influence of ovarian architecture on the organization and outcome of follicles within the ovary, both the origin of the cortical and medullary compartments and the

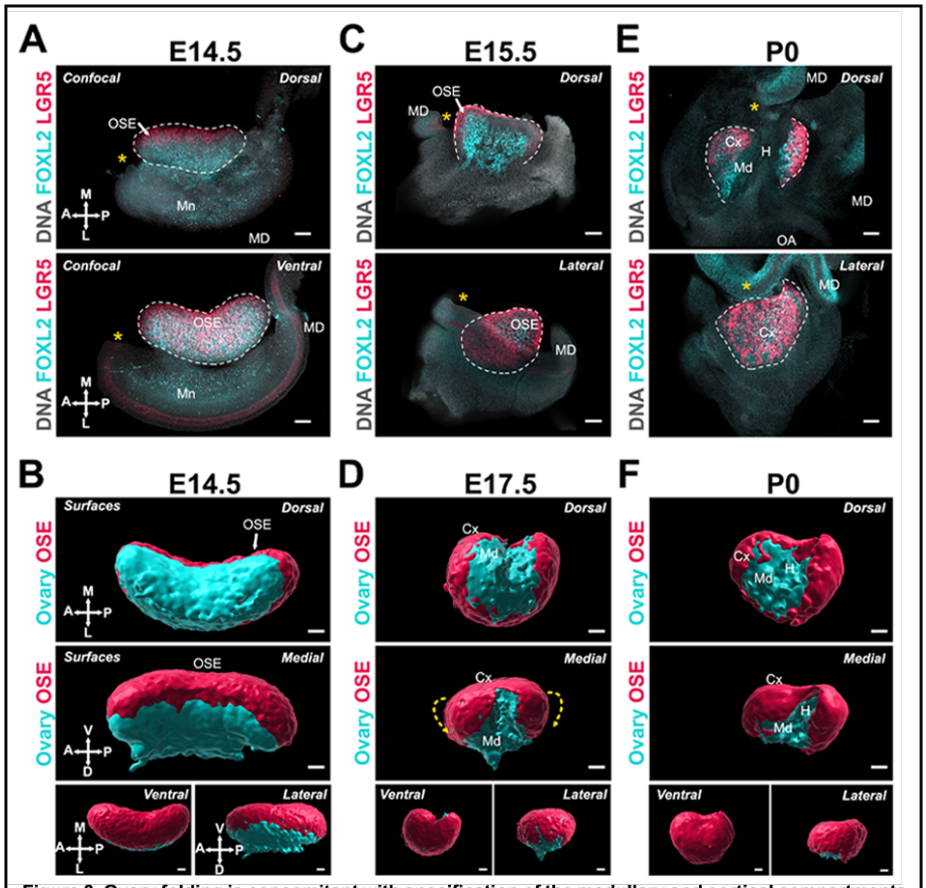

Figure 3. Ovary folding is concomitant with specification of the medullary and cortical compartments of the ovary. (**A, C, E**) Optical sections from confocal Z-stacks of whole ovary/mesonephros complexes from *Lgr5-Gfp* mice at E14.5, E15.5 and P0 immunostained for GFP (*red*) and FOXL2 (*cyan*), and counter-stained with Hoechst nuclear dye (*grayscale*). Images in the top row were taken from the dorsal side and the bottom row from the ventral (E14.5) or lateral (E17.5; P0). Yellow asterisks indicate the location of the infundibulum of the presumptive oviduct for reference. (**B, D, F**) 3D models generated by isosurface segmentation of lightsheet images taken of whole ovaries from *Lgr5-Gfp* mice at E14.5, E17.5 and P0 immunostained for FOXL2 (*cyan*) and GFP (*red*). Top panels represent the dorsal view, middle panels represent the medial view, and small bottom panels illustrate ventral and lateral views of the same ovary. Yellow dashed arrows in D indicate the wrapping of the OSE from the ventral to the dorsal side of the ovarian domain. White arrows point to the ovarian surface epithelium (OSE). Mn, mesonephros; MD, Müllerian duct; Md, medulla; Cx, cortex; H, hilum. Compasses on the bottom left of each panel indicate the orientation of the ovary for the entire row: V, ventral; L, lateral; D, dorsal; M, medial; A, anterior; P, posterior. Scale bars, 100μm.

nature of the signals and the mechanisms that drive this differential patterning remain unclear. The process of ovary folding as well as the differences in the conformation of the ventral and dorsal surfaces of

the ovary led us to investigate whether ovary folding is responsible for the regionalization of the ovary into cortical and medullary compartments. The ovarian cortex is covered with ovarian surface epithelium (OSE), which is the female-specific derivative of the gonadal coelomic epithelium. We used the dynamics of the OSE to serve as a proxy for the establishment of the ovarian cortex during morphogenesis using the *Lgr5-GFP-IRES-CreER* (*Lgr5-Gfp*) transgenic reporter, in which cells of the OSE are labelled with GFP (red in these images) (Fig. 3) (Ng et al., 2014). At E14.5, the OSE was only visible in the most medial aspect of the ovary from the dorsal side but covered the ventral portion of the ovarian surface, as demonstrated by the overlap of FOXL2 staining and GFP expression (Fig. 3A, B). The OSE continued to cover the ventral and lateral faces of the ovary throughout the time-course (Fig. 3C-F). From E15.5 to P0, the OSE became more visible from the dorsal side as the anterior and posterior domains folded toward the center. As this occurred, the FOXL2+/LGR5- domain became gradually restricted to the dorsal extrusion of the ovarian domain, and to the middle region of the ovary from the dorsal face (Fig. 3C-F). The appearance of the LGR5+ domain on the dorsal side coincided with the inflexion of the middle region of the ovary, which presumably resulted in an internalization of the cells originally present on the dorsal surface of the ovary to form the ovarian medulla, and to establish the hilum, which serves as a conduit for ovary vasculature and innervation (Fig. 3D, E, F).

The expansion and relocation of the Müllerian duct leaves the ovary fully encapsulated.

Having characterized the structural changes of the ovarian domain, we next investigated the developmental dynamics of tissues closely associated with the ovary, starting with the Müllerian duct. The invagination and elongation of the Müllerian duct occurs from E11.5 to E13.5 in the mouse and is followed by a significant expansion of the duct and functional regionalization into oviduct, uterus, and vagina (Kobayashi and Behringer, 2003; Roly et al., 2018). The presumptive oviduct develops closest to the ovary and undergoes coiling during late gestation (Ford et al., 2020; Harwalkar et al., 2021). We investigated the correlations between the dramatic changes in oviduct conformation and ovary morphogenesis. For this, we first used 3D reconstructions of the ovary and Müllerian duct based on isosurface segmentation of lightsheet images of FOXL2 and PAX8 immunostaining respectively. The shift in position of the Müllerian duct with respect to the ovary was best visualized from caudal and cranial views (Fig. 4A). At E14.5, the Müllerian duct was fully invaginated and lay parallel to the entire longitudinal axis of the ovary, on its dorso-lateral aspect (Fig. 4A). The infundibulum is the cranial opening of the presumptive oviduct, which in adults is responsible for capturing ovulated oocytes. The infundibulum was initially located near the anterior pole of the ovary (Fig. 4A - *yellow asterisk*). At E17.5, while the infundibulum had only slightly shifted to the ventro-medial region of the ovary and the presumptive uterus remained parallel to the longitudinal axis of the ovary, the presumptive oviduct had expanded and shifted ventrally to the ovary (Fig. 4A). This shift was more pronounced in the anterior region of the oviduct (Fig. 4A). By P0, the presumptive oviduct had significantly expanded and coiled into its characteristic structure, and this was associated with a complete shift to the ventral side of the ovary (Fig. 4A).

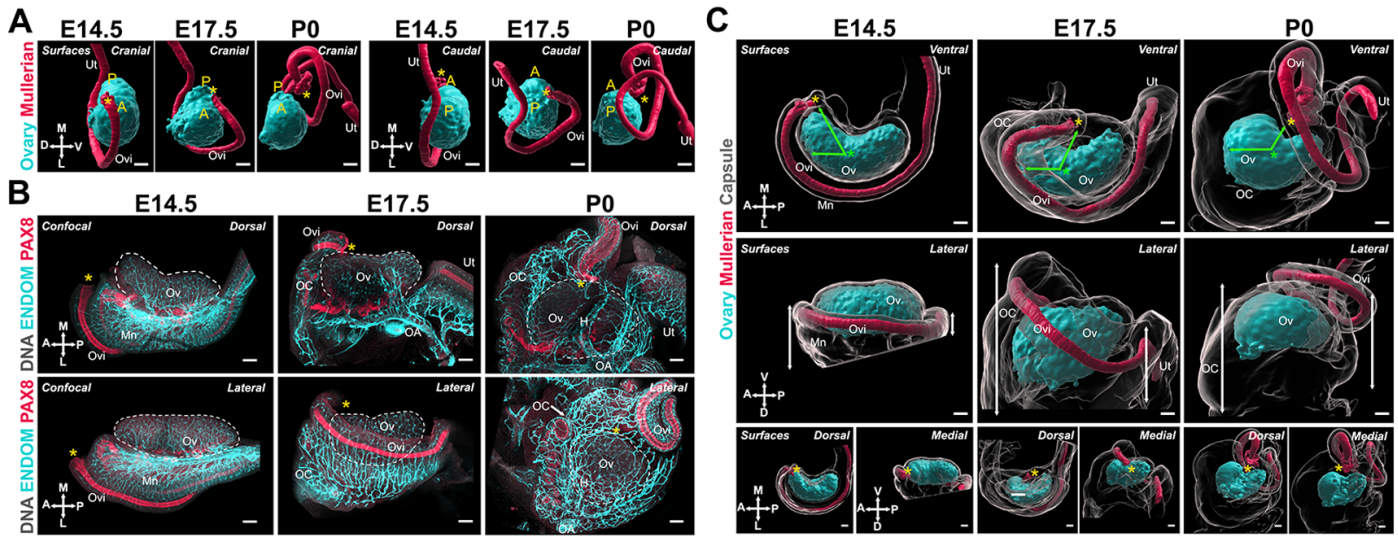

Figure 4. The expansion and relocation of the Müllerian duct leave the ovary fully encapsulated. (**A**) 3D model generated by isosurface segmentation of lightsheet images taken of whole ovaries at E14.5, E17.5 and P0 immunostained for FOXL2 (*cyan*) and PAX8 (*red*). A, anterior pole; P, posterior pole. (**B**) Maximum intensity projections from confocal Z-stacks of whole ovary/mesonephros complexes at E14.5 (**B**, *left*), E17.5 (**B**, *middle*) and P0 (**B**, *right*) immunostained for PAX8 (*red*) and ENDOMUCIN (*cyan*), and counterstained with Hoechst nuclear dye (*grayscale*). Images in the top row were taken from the dorsal side and the bottom row from the lateral side. (**C**) 3D models generated by isosurface segmentation of lightsheet images taken of whole ovaries at E14.5 (**C**, *left*), E17.5 (**C**, *middle*), and P0 (**C**, *right*) immunostained for FOXL2 (*cyan*) and PAX8 (*red*), and counterstained with Hoechst nuclear dye (*grayscale*). The isosurfaces generated with the gray channel allow for visualization of the entire tissue, including the ovarian capsule. White arrowheads point to the Hoechst-based surface of the ovary, which extends beyond the FOXL2+ domain, and should not be confused with the ovarian capsule. Top panels represent the ventral view, middle panels represent the lateral view, and small bottom panels illustrate dorsal and medial views of the same ovary. Green arrows indicate the change in position of the infundibulum relative to the longitudinal plane of the ovary. Green asterisks indicate the approximate center of the ovary. White double arrows indicate the extension of mesonephric tissue around the ovary in the anterior (*left arrows*) and posterior regions (*right arrows*). Yellow asterisks indicate the location of the infundibulum of the presumptive oviduct for reference. Ut, uterus; Ovi, oviduct; Ov, ovary; OC, ovarian capsule; Mn, mesonephros; MD, Müllerian duct; OA, ovarian artery, H, hilum. Compasses on the bottom left of each panel indicate the orientation of the ovary for the entire row: V, ventral; L, lateral; D, dorsal; M, medial; A, anterior; P, posterior. Scale bars, 100µm.

We next investigated how the relocation of the Müllerian duct correlated with ovary encapsulation. We immunostained whole-mount gonads with antibodies against PAX8 to label the epithelium of the Müllerian duct and ENDOMUCIN to label the vasculature (Brachtendorf et al., 2001), as a way to visualize the highly vascularized ovarian capsule. These samples were imaged with confocal microscopy (Fig. 4B). In parallel, we used 3D reconstructions of the ovary, Müllerian duct, and ovarian capsule based on isosurface segmentation of lightsheet images of FOXL2, PAX8 and Hoechst labelling, respectively. Consistent with results shown in figure 4A, at E14.5, the Müllerian duct was located immediately below the ovary, with the infundibulum on the lateral side, near the anterior pole (Fig. 4B, *left*; C, *left*). At this stage, the ovary was in direct contact with the abdominal cavity and was not encapsulated. Both the mesonephros and ovary were already highly vascularized (Fig. 4B*a*). We used isosurface segmentation of the Hoechst labelling in our lightsheet images to generate surfaces representing the entire ovary/mesonephros complex (Fig. 4C - *grayscale*) and transparency to make the FOXL2-positive ovarian domain visible (Fig. 4C - *cyan*). Note that the FOXL2 domain is surrounded by the OSE (not labelled in these images), which accounts for the space between the Hoechst-based isosurface and the FOXL2 domain at all stages (Figure 4C - *white arrows*) and should not be confused with the ovarian capsule, which is absent at E14.5. At E17.5, the infundibulum had progressed from the lateral to the medial portion of the ovary, and had begun travelling away from the anterior pole to the center of the ovary (Fig. 4B*, middle*; C*, middle*). This was associated with a lateral to medial expansion of cranial mesonephric tissue, the presumptive ovarian capsule, that began covering the cranial region of the ovary (Fig. 4C, *middle - green arrows*). At this stage, the middle portion of the Müllerian duct wrapped around the latero-ventral side of the ovary and was no longer visible from the dorsal perspective (Fig. 4B*, middle*). Thus, the process was best visualized from the lateral view, where the cranial region of the ovary was no longer

directly accessible from the abdominal cavity but was instead covered by highly vascularized mesonephric tissue, lined on the medial edge by the expanding Müllerian duct (Fig. 4B*, middle*; C, *middle*). By P0, the infundibulum had continued its cranial to caudal progression and was now located at the middle of the medial side of the ovary, near the opening of the hilum (Fig. 4B*, right*; C*, right*). This change was associated with a continued expansion of cranial mesonephric tissue, which now covered the cranial half of the ovary. At this stage, we also observed a caudal expansion of tissue, and the uterus was now aligned with the infundibulum on the medial side of the ovary (Fig. 4B*, right*). From the ventral side, the P0 ovary appeared fully encapsulated, with the coils of the oviduct forming the ventral rim of the ovarian capsule (Fig. 4C*, right*). By the end of this process, the infundibulum of the oviduct was embedded in the capsule, where it later will be responsible for capturing ovulated oocytes.

These data demonstrate that the encapsulation of the ovary occurs during late gestation and is intimately associated with the expansion and regionalization of the Müllerian duct to form the oviduct. This observation prompted us to investigate potential mechanical components that could be affecting structural change in both the ovary and the oviduct simultaneously.

The broad ligament and cranial suspensory ligament tether the ovary to the Müllerian duct and body wall and may act as mechanical drivers of ovary folding and encapsulation.

The position of the ovary within the body cavity is maintained by two ligaments: the broad ligament (BL) and the cranial suspensory ligament (CSL). The BL and CSL are peritoneal folds that support the uterus, oviduct, and ovary, providing a conduit for vasculature, innervation, and lymphatics, and securing the position of the reproductive organs inside the body (Martin et al., 1996). While the BL is a single continuous structure, different segments are defined by the organs they support: the mesometrium supports the uterus, the mesovarium supports the ovary, and the mesosalpinx supports the oviduct. The caudal end of the BL is tethered to the dorsal pelvic body wall, while its cranial region transitions into the CSL, which tethers the ovary to the dorsal abdominal body wall near the diaphragm (Hutson et al., 1997; van der Schoot and Emmen, 1996). Because these structures are fibromuscular tethers of the ovary, we postulated that developmental dynamics of the BL and CSL could provide insight into the mechanisms of ovary morphogenesis. We first used immunostaining against the neural marker TUJ1 as a proxy for visualizing the BL in whole urogenital complexes from E15.5 to E18.5 (Fig. 5A). We found that the mesometrium, mesovarium, and mesosalpinx formed a continuous structure on the medial/dorsal aspect of the reproductive tract and ovary at E15.5 and E14.5 (Fig. 5A, *left;* C, *left*) labeled also with alpha smooth muscle actin (aSMA) (Fig. S2A, *left*). At E16.5, the mesovarium was visible as a thin sheet of tissue on the medial/dorsal surface of the ovary that hosted neural projections (Fig. 5A, *middle*) and vasculature (Fig. S2A, *middle*) growing towards the ovary. At E18.5, this sheet of tissue was no longer visible on the medial/dorsal surface of the ovary, and innervation and vasculature had penetrated the dorsal ovary in the region of the hilum (Fig. 5A, *right*; Fig. S2A, *right*). These observations suggested that the mesovarium, and associated extrinsic components, became internalized into the ovarian medulla as the ovary folded. We next focused on the development of the CSL, which we labelled with antibodies

against TNC and aSMA in urogenital complexes from Tg*(Nr5a1-GFP)* mice (Stallings et al., 2002), referred to here as *Sf1-eGFP*, in which both the gonad and adrenal are labelled with GFP (Fig. 5B). We found that at E14.5, the CSL was tightly associated with the initial site of invagination of the MD and extended cranially to the ovary, along the kidney and up to the adrenal (Fig. 5B, *left*). The adrenal derives from a subpopulation of cells that segregate from gonadal cells early in gonad formation (Saito et al., 2017; Upadhyay and Zamboni, 1982), suggesting that the TNC+ CSL links these two organs prior to their separation, and throughout development. At P0, the aSMA-labelled CSL remained closely associated with the ovary, kidney, and adrenal (Fig. 5B, *right*). By this stage, the kidney had significantly grown in volume, resulting in a longer distance between the ovary and adrenal, and we propose that this growth exerts mechanical tension in the CSL. To investigate the link between the CSL, ovary, and MD in more detail, we labelled isolated gonad/mesonephros complexes at E14.5 and found that the TNC+ domain lined the medial ridge of the ovary and the medial edge of the infundibulum before extending towards the dorsal

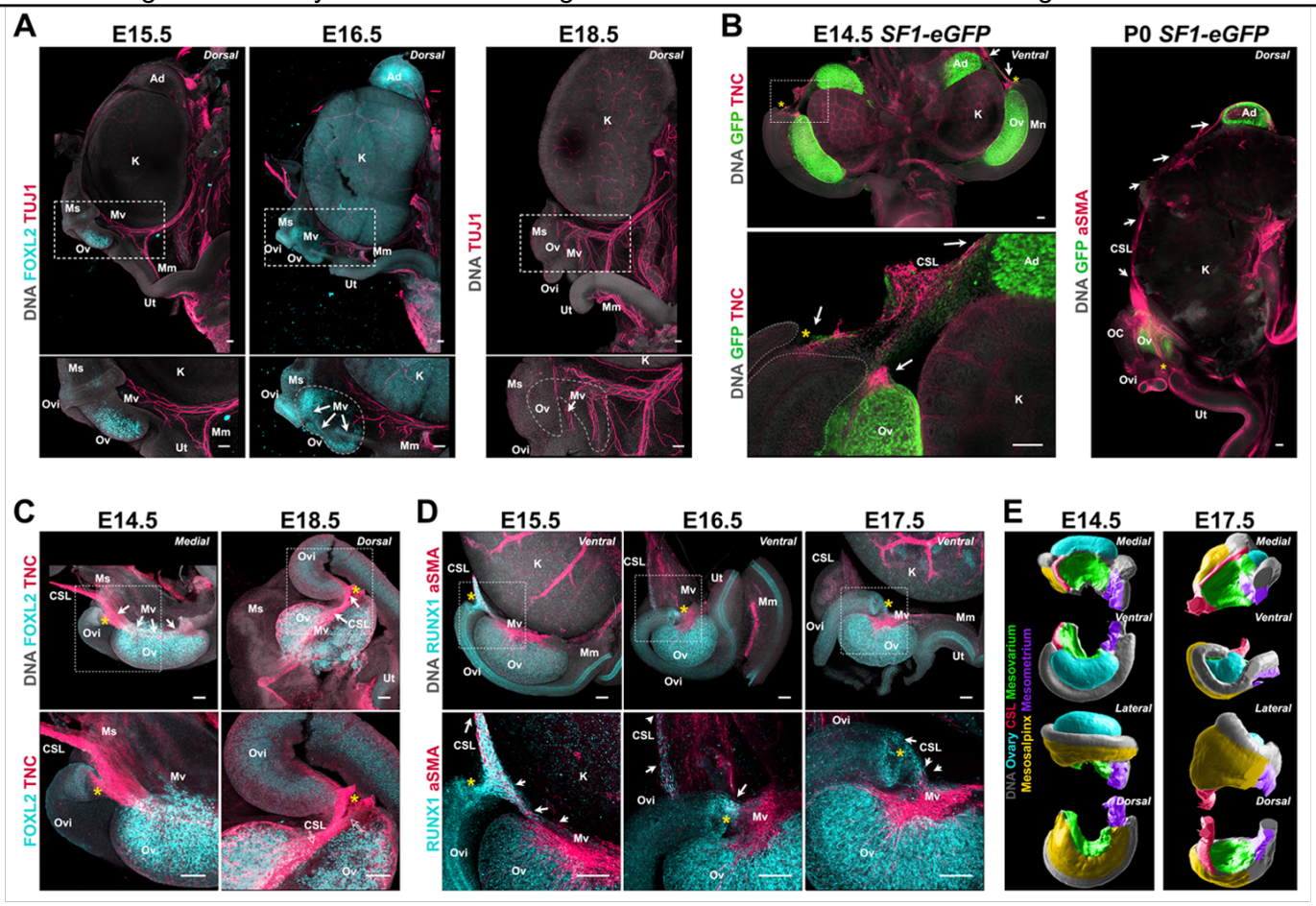

Figure 5. Developmental dynamics of the ovarian ligaments correlate with ovary morphogenesis. (**A**) Maximum intensity projections from confocal Z-stacks of whole urogenital complexes at E15.5, E16.5 and E18.5 immunostained for TUJ1 (*red*) and FOXL2 (*cyan* - left and middle panel only), and counterstained with Hoechst nuclear dye (*grayscale*). Images on the bottom row are close-ups of the regions outlined in the top row images. (**B**) Maximum intensity projections from confocal Z-stacks of the whole urogenital complex of XX Sf1-eGFP mice at E14.5 (*left*) and P0 (*right*), immunostained for GFP (*green*) and TNC (E14.4, *red*) or aSMA (P0, *red*), and counterstained with Hoechst nuclear dye (*grayscale*). The E14.5 sample was imaged from the ventral side and the P0 from the dorsal. The left bottom panel on the left is a high magnification view of the area outlined in the left top left panel. White arrows point to the continuity of the CSL from the ovary to the adrenal. (**C**) Maximum intensity projections from confocal Z-stacks of whole ovary/mesonephros complexes at E14.5 and E18.5 immunostained for FOXL2 (*cyan*) and TNC (*red*), and imaged from the medial side. White arrows point to the continuity of the CSL between the medial ridge of the ovary and the infundibulum. (**D**) Maximum intensity projections from confocal Z-stacks of whole ovary/mesonephros complexes at E15.5, E16.5, and E17.5 immunostained for RUNX1 (*cyan*) and aSMA (*red*), and imaged from the ventral side. White arrows point to the population of RUNX1+ cells linking the medial edge of the mesovarium to the infundibulum, and to the CSL. (**E**) 3D models generated by isosurface segmentation of lightsheet images taken of whole ovary/mesonephros complexes at E14.5 (*left*) and E17.5 (*right*) stained with Hoechst nuclear dye (*grayscale*), and false-colored to illustrate the three regions of the BL (*purple*, mesometrium; *yellow*, mesosalpinx; *green*, mesovarium), the CSL (*red*), and the ovary (*cyan*). Each row represents a different view of the same ovary for each stage (from top to bottom: medial; ventral; lateral; dorsal). Yellow asterisks indicate the location of the infundibulum of the presumptive oviduct for reference. Ad, adrenal; CSL, cranial suspensory ligament; K, kidney; Mn, mesonephros; Mm, mesometrium; Ms, mesosalpinx; Mv, mesovarium; OC, ovarian capsule; Ov, ovary; Ovi, oviduct; Ut, uterus. Scale bars, 100µm.

abdominal wall (Fig. 5C, *left*). At E18.5, the ovary had folded and the TNC+ CSL continued to line the medial edge of the infundibulum, which had relocated to the opening of the ovarian hilum (Fig. 5C, *right* -

yellow asterisk; Fig. S2B). However, at this stage, the CSL was no longer parallel to the longitudinal axis of the ovary but instead ran through the middle of the ovary before extending towards the dorsal abdominal wall (Fig. 5C, *right*). These observations were confirmed in semi-transparent 3D models of the ovary and CSL based on lightsheet images, where the ovary was seen folding around the CSL between E14.5 and P0 (Fig. S2B). Thus, rearrangements of the CSL correlated with folding of the ovarian domain and relocation of the infundibulum. Using IF labeling for RUNX1, which is known to label granulosa cells of the ovary and epithelial cells of the Müllerian duct (Laronda et al., 2013; Nicol et al., 2019), we discovered that RUNX1 also labels a discrete population of cells present at the medial edge of the aSMA+ mesovarium, which appeared to form a continuous structure from the mesovarium to the infundibulum to the body wall from E14.5 to E17.5 (Fig. 5D). These data suggest that the CSL acts as a physical tether that links the ovary to the infundibulum and to the body wall throughout development. Therefore, any mechanical tension on the CSL, caused for example by the growth of the kidney, could direct the relocation of the infundibulum and the folding of the ovarian domain simultaneously. The false-colored 3D models in Figure 5E represent all four views of ovary/mesonephros complexes at E14.5 and E17.5, and clearly illustrate the expansion of the mesosalpinx that correlates with translocation of the Müllerian duct, and results in ovary encapsulation (Fig. 5E, *yellow*) and internalization of the mesovarium during ovary folding (Fig. 5E, *green*).

Developmental dynamics of the rete ovarii are integrated with events of ovary morphogenesis.

The rete ovarii (RO) is an epithelial appendage of the ovary thought to arise from the mesonephric tubules (Satoh, 1985). The RO was first described in 1870 by W. Waldeyer (as cited by Byskov and Lintern-Moore, 1973), and was believed to be a functionless female homologue of the male rete testis (Kulibin and Malolina, 2020; Wenzel and Odend'hal, 1985). It was once thought to degenerate in most individuals, however research shows that this structure persists into adulthood in large mammals (Archbald et al., 1971; Hadek, 1958; Mossman and Duke, 1975). The RO consists of three distinct regions: (1) the intraovarian rete (IOR), (2) the connecting rete (CR), and (3) the extraovarian rete (EOR) (Byskov, 1978). The IOR resides inside of the ovary and consists of thin strings of squamous cells. The EOR is a tubular epithelial structure that resides outside of the ovary, and the CR is a transitional zone between the two regions (Byskov and Lintern-Moore, 1973; Lee et al., 2011). Previous literature has not explored the development of the RO or a possible role during morphogenesis of the ovary.

As the RO is directly linked to the ovary, we hypothesized that morphogenesis of the RO might be involved in morphogenesis of the ovary. To investigate the morphological changes of the RO during development, we used antibodies against PAX8, which labels all three RO regions, to image the ovary and RO using confocal and lightsheet microscopy. Our findings demonstrated that the regions of the RO changed in proportion to one another during the embryonic and early postnatal period. At E14.5, the RO was exclusively located on the dorsal side of the ovary and all three regions were distinguishable (Fig. 6A*, E14.5*; B*, left*). The IOR was the largest of the three regions at this stage and lined most of the interface between the ovary and mesonephros. PAX8+ cells were squamous and intermingled with FOXL2+ cells,

suggesting the IOR was embedded inside the ovarian domain. The rest of the structure was connected to the IOR and located within the mesonephric tissue. The region proximate to the ovary was characterized by a short region of transition from squamous epithelial cells in the CR to a columnar epithelium in the EOR, which extended in tubules outward from the ovary (Fig. 6A*, E14.5*; B*, left*). As the ovary folded between E16.5 and E17.5, the IOR adopted a U-shape (Fig. 6A*, E16.5-E17.5*; B*, middle*). At E16.5, the tubules of the EOR began to elongate and by E17.5 had wrapped around to the ventral face of the ovary (Fig. 6A, *E16.5-E17.5*; B, *E17.5*). The CR was located alongside the dorsal protrusion of the ovary of this stage (Fig. 6A*, E16.5*; B*, middle*). At E17.5, the embedded IOR was restricted to the edge of the FOXL2 domain on the dorsal side (Fig. 6A*, E17.5*), and the CR was more predominant with growth of the dorsal protrusion. The EOR underwent rapid growth and convolution of the tubules, especially apparent in the 3D model, where both the dorsal and medial views demonstrated the intricacy of the tubular coiling (Fig. 6B*, right*). By E18.5, the IOR had slightly regressed compared to E17.5, and no longer extended all the way to the poles of the ovarian domain (Fig. 6A*, E18.5*). At this stage, the EOR was the largest of the three regions, and had developed into an elaborate and convoluted tubular structure that curved alongside the ovary within the ovarian capsule (Fig. 6A*, E18.5*). Between P0 and P5, the IOR mostly regressed to the lateral edge of the medulla, but a thin string of cells continued to line the dorsal boundary between the ovarian cortex and medulla, and the EOR continued to grow and wrap around the ovary (Fig. 6A, *P0-P5*; B, *right*). The location of the IOR at the boundary of the ovarian cortex coincides with the dorsal opening of the hilum. To further characterize this domain, we stained late-gestation ovaries for ENDOMUCIN and TUJ1, which label vasculature and innervation respectively. These components entered the ovary through this dorsal opening, lined with cells of the IOR (Fig. S3A, B). This suggests that the IOR plays a role in the invasion of extrinsic components into the ovarian medulla, either by mechanically restricting folding on the dorsal side, by producing chemoattractant signals, or both.

The morphological difference between cells of the EOR and CR/IOR prompted us to investigate the expression of tubular epithelium markers KRT8 and E-Cadherin. We found that these markers were significantly enriched in the EOR (Fig. S4A, B). The EOR was also the only region to be wrapped in a aSMA+ sheath, presumably fibromuscular tissue of mesenchymal origin (Fig. S4C). We also used antibodies against SOX9, a broader epithelial marker, and noted that all three regions of the RO were labelled (Fig. S4D). A small subset of the CR and IOR cells were positive for the pre-granulosa marker FOXL2, suggestive of a transitional region. The CR and IOR also expressed several ovarian markers, including RUNX1, SF-1 and GATA4, reinforcing the notion that cells of the IOR are closely related to ovarian cells (Fig. S4E, F, G). This is consistent with a recent single-cell transcriptomic study of mouse gonad development showing that cells of the rete ovarii were closely related to pre-supporting cells, and even gave rise to a subset of pre-granulosa cells during during early differentiation of the ovary (Mayère et

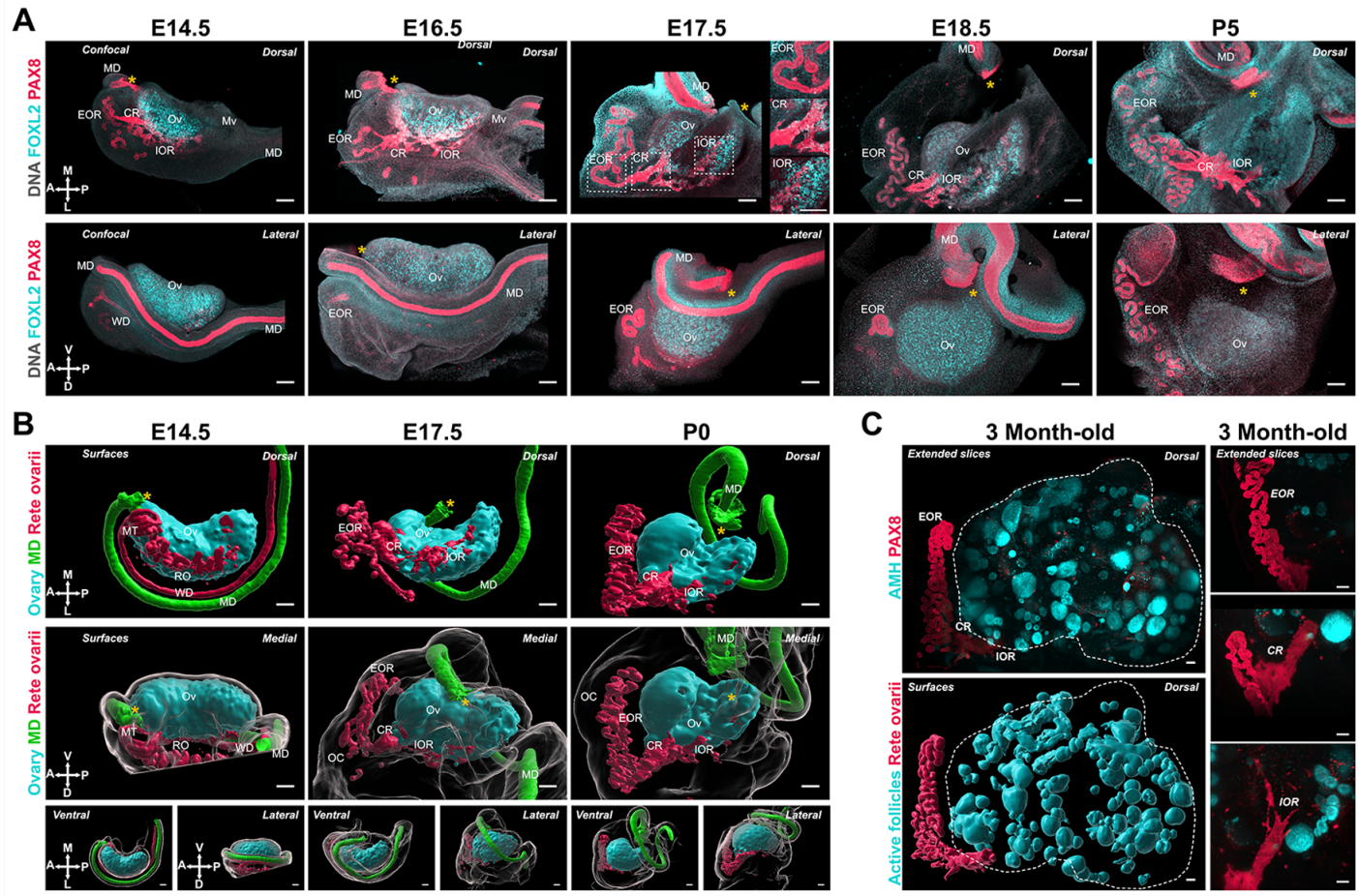

Figure 6. Developmental dynamics of the rete ovarii correlate with ovary morphogenesis. (**A**) Maximum intensity projections from confocal Z-stacks of whole ovary/mesonephros complexes at E14.5, E16.5, E17.5, E18.5, and P5, immunostained for FOXL2 (*cyan*) and PAX8 (*red*), and counterstained with Hoechst nuclear dye (*grayscale*). Samples in the top row were imaged from the dorsal side and samples from the bottom row from the lateral side. Side panels in (**A**, E17.5) are close-ups of the three regions of the RO outlined at E17.5 (from top to bottom: EOR, CR, and IOR). (**B**) 3D models generated by isosurface segmentation of lightsheet images taken of whole ovaries at E14.5, E17.5 and P0 immunostained for FOXL2 (*cyan*) and PAX8 (Müllerian duct, *green*; and Rete ovarii, *red*). All samples were counterstained with Hoechst nuclear dye (*grayscale*). Top panels represent the dorsal view, middle panels represent the medial view, and small bottom panels illustrate ventral and lateral views of the same ovary. Yellow asterisks indicate the location of the infundibulum of the presumptive oviduct for reference. Compasses on the bottom left of each panel indicate the orientation of the ovary: V, ventral; L, lateral; D, dorsal; M, medial. (**C**) Lightsheet images of whole ovaries from 3-month-old mice immunostained for AMH (*cyan*) and PAX8 (*red*). The top panel shows the Imaris 'extended slice' view of the native image, while the bottom panel illustrates the 3D surfaces of the RO (PAX8, *red*) and ovarian follicles (AMH, *cyan*) generated by isosurface segmentation of the same image. Images in the right panel are close-ups of the three regions of the RO in an adult ovary: from top to bottom: EOR, CR, IOR. CR, connecting rete; EOR, extraovarian rete; IOR, intraovarian rete; MD, Müllerian duct; Mn, mesonephros; MT, mesonephric tubules; Mv, mesovarium; OC, ovarian capsule; Ov, ovary; RO, rete ovarii; WD, Wolffian duct. Scale bars, 100µm.

al., 2021). While expression of RUNX1 was lower in the CR, this was the only gonadal marker to be expressed in the tubular cells of the EOR (Fig. S4E). In addition, we found that some cells of the IOR and CR expressed both PAX8 and the gonadal markers *Nr5a1* (SF1-eGFP) and FOXL2 (Fig S4F, H - *white arrows*). Interestingly, PAX8+ cells of the IOR were observed in close contact with oocytes labeled with

HuC/D, suggesting that the IOR was intermingled with ovarian follicles in the medullary region (Fig. S4H). We then investigated the presence and structure of the RO in adult mouse ovaries using tissue clearing and lightsheet microscopy. The RO was labelled with PAX8 antibodies, and the ovarian domain was identified using antibodies against AMH (Anti-Müllerian Hormone - a marker of preantral and antral follicles). All three regions of the RO persisted into adulthood (Fig. 6C), suggesting that the role of the RO is not limited to the embryonic period. In adulthood, the EOR remained the largest of the regions followed by the CR and IOR (Fig. 6C).

Combinations of* Pax2 *and* Pax8 *deletion alleles differentially affect the oviduct and regions of the rete ovarii.

Pax2 and *Pax8* are essential genes during the development of the urogenital system, and null alleles for both of these have been shown to impact development of the kidneys and the reproductive ducts in mice (Torres et al., 1995, Mittag et al., 2007). While Pax8 is expressed in all three regions of the rete ovarii, Pax2 is not expressed in the intraovarian progenitors of the rete ovarii (Mayere et al., 2022). Both genes are expressed in cells of the oviduct throughout development (Torres et al., 1995;). Thus, to directly test the role of proximate tissues on ovary morphogenesis, we established a genetic model for ubiquitous deletion of *Pax2* and *Pax8*. We first generated an allelic series and immunostained ovary/oviduct complexes with antibodies against KRT8 and PAX8 to study the impact of loss of *Pax2*, *Pax8*, or both, on the oviduct and the rete ovarii at E18.5 (Fig. 7A). The oviduct appeared unaffected by the absence of one copy of either *Pax2* or *Pax8* (Figure 7A, *top row-second and third columns*). While deletion of a single copy of *Pax2* ($Pax2^{del/+}$; $Pax8^{+/+}$) did not appear to impact the oviduct or any region of the RO (Fig. 7A, *middle and bottom row-second column*), deletion of a single copy of *Pax8* ($Pax2^{+/+}$; $Pax8^{del/+}$) led to a decrease in the size of the IOR and the CR, which was no longer connected to the EOR (Fig. 7A, *bottom row-third column*). When one copy of *Pax2* and one copy of *Pax8* were deleted ($Pax2^{del/+}$; $Pax8^{del/+}$), the Müllerian duct began to display perturbations, such as gaps in the epithelium or a blunt end near the uterus (Fig. 7A, *fourth column, white arrows*). In addition, all three regions of the RO were affected: the IOR and CR were diminished similarly to $Pax2^{+/+}$; $Pax8^{del/+}$ samples, and the EOR was sparse with less convoluted tubules (Fig. 7A, *fourth column, middle and bottom rows*). Homozygous deletion of *Pax2* ($Pax2^{del/del}$; $Pax8^{+/+}$) or *Pax8* ($Pax2^{+/+}$; $Pax8^{del/del}$) severely affected the oviduct, which displayed large gaps and blunt distal ends. However, in both cases, a significant portion of the oviduct proximal to the ovary was continuous (Fig. 7A, *top row-fifth and sixth column*). While the IOR and CR persisted in animals with homozygous deletion of *Pax2* ($Pax2^{del/del}$; $Pax8^{+/+}$), the EOR was absent. In contrast, all three regions of the RO were affected by homozygous deletion of *Pax8*: the IOR and CR were completely absent, while the EOR appeared fragmented (Fig. 7A, *middle and bottom row-sixth column*). To summarize, this allelic series shows that development of a continuous oviduct and EOR requires two functional copies of either Pax2 or Pax8 plus one functional copy of the other (Table S1). The intraovarian and connecting regions of

the RO do not require expression of *Pax2*, nor does *Pax2* compensate for loss of *Pax8* in these regions (Table S1). Both copies of *Pax8* are required to form the IOR, while one copy is sufficient for development of the CR (Table S1). Importantly, all ovaries from this allelic series were encapsulated and ovary folding was not obviously affected, suggesting that these morphogenetic processes do not rely on the presence of a continuous oviduct or the rete ovarii at E17.5.

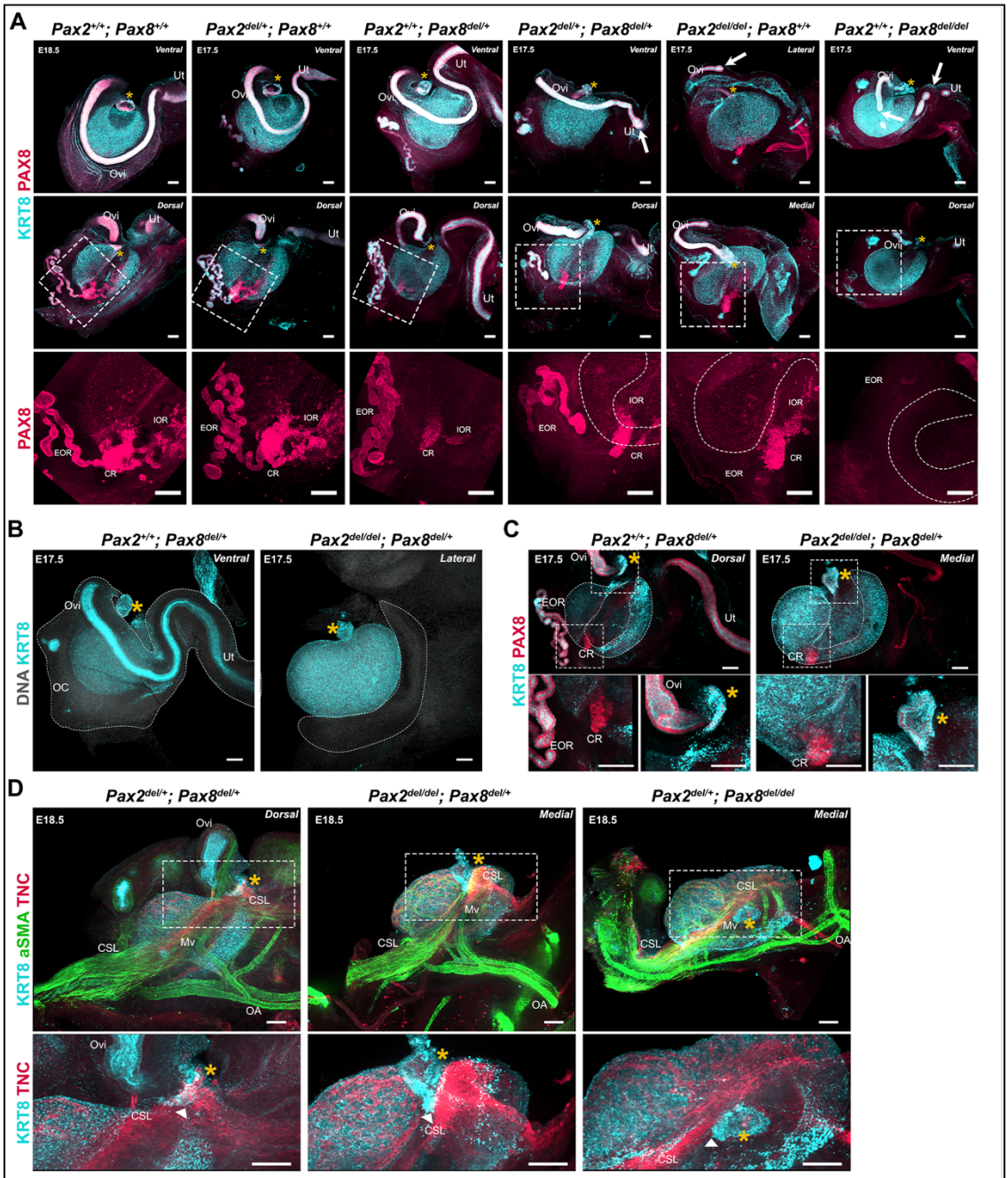

Figure 7. Perturbations of the Müllerian Duct and rete ovarii by deletion of *Pax2* and/or *Pax8* disrupt ovary morphogenesis. Perturbations of the Müllerian Duct and rete ovarii by deletion of *Pax2* and/or *Pax8* disrupt ovary morphogenesis. (**A**) *Pax2/Pax8* deletion allelic series. Maximum intensity projections from confocal Z-stacks of whole ovary/mesonephros complexes at E17.5 and E18.5, immunostained for KRT8 (*cyan*) and PAX8 (*red*). Each sample is representative of the phenotype observed for different combinations of *Pax2* and *Pax8* deletion alleles. Images in the top row were captured from the dorsal side, and images in the middle and bottom row from the dorsal side. Images in the bottom row are close-ups of the regions outlined in the middle row. White arrows point to disruptions of the Müllerian duct. Dashed lines in the bottom row represent the KRT8+ cortical domain of the ovary. (**B**) The segment of the oviduct is required for ovary encapsulation. Maximum intensity projections from confocal Z-stacks of whole ovary/mesonephros complexes at E17.5, immunostained for KRT8 (*cyan*) and counterstained with Hoechst nuclear dye (*grayscale*). The dashed outline represents the ovarian capsule, which is absent in $Pax2^{del/del}$; $Pax8^{del/+}$ samples. (**C**) Only the infundibulum and connecting rete persist in $Pax2^{del/del}$; $Pax8^{del/+}$ samples. Maximum intensity projections from confocal Z-stacks of whole ovary/mesonephros complexes at E17.5, immunostained for KRT8 (cyan) and PAX8 (red). Images in the bottom row are close-ups of the regions outlined in the top row: left, rete ovarii; right, infundibulum. (**D**) The cranial suspensory ligament remains tethered to the infundibulum remnant in $Pax2^{del/del}$; $Pax8^{del/+}$ and $Pax2^{del/+}$; $Pax8^{del/del}$ samples. Maximum intensity projections from confocal Z-stacks of whole ovary/mesonephros complexes at E18.5, immunostained for KRT8 (cyan), aSMA (green), and TNC (red). Images in the bottom row are close-ups of the regions outlined in the top row. White arrowheads point to the attachment of the CSL to the infundibulum. Yellow asterisks indicate the location of the infundibulum of the presumptive oviduct for reference. CR, connecting rete; CSL, cranial suspensory ligament; EOR, extraovarian rete; IOR, intraovarian rete; Mv, mesovarium; OA, ovarian artery; OC, ovarian capsule; Ov, ovary; Ovi, oviduct, Ut, uterus. Scale bars, 100μm.

While a segment of oviduct is required for ovary encapsulation, the infundibulum is sufficient to tether the ovary to the cranial suspensory ligament.

We next examined the development of the RO and Müllerian duct in *Pax2*$^{del/del}$*; Pax8*$^{del/+}$ fetuses. We first noted that *Pax2*$^{del/del}$*; Pax8*$^{del/+}$ and *Pax2*$^{del/+}$*; Pax8*$^{del/del}$ presented with kidney agenesis (Fig. S5), consistent with the phenotypes previously observed using combinations of null alleles for *Pax2* and *Pax8* (Bouchard et al., 2002; Laszczyk et al., 2020; Torres et al., 1995). We found in these samples that the ovaries were located higher in the body cavity, much closer to the adrenal than in controls (Fig. S5). This suggests that growth of the kidney pushes the ovary to a more caudal position during development. Using antibodies against KRT8 to label the Müllerian epithelium, we found that *Pax2*$^{del/del}$*; Pax8*$^{del/+}$ mice lacked most of the Müllerian duct, including the segment of the oviduct that typically wraps around the ovary (Fig. 7B, Table S1). This was associated with absence of the ovarian capsule, demonstrating that a continuous oviduct is required for growth of the mesosalpinx that leads to ovary encapsulation (Fig. 7B, Table S1). We next examined the expression of PAX8 and KRT8 on the dorsal side of *Pax2*$^{del/del}$*; Pax8*$^{del/+}$ ovaries compared to single deletion of *Pax8* (*Pax8*$^{del/+}$), and found that the IOR and EOR were absent, while a fragment of the CR persisted (Fig. 7C, Table S1). In addition, we observed a small fragment of KRT8+/PAX8+ tissue located at the medial opening of the folded ovary (Fig. 7C - *top and bottom right panels*). The location and immunolabeling indicated that this was the infundibulum of the oviduct, which persisted despite the deletion of both copies of *Pax2* and one copy of *Pax8*. Interestingly, the position of the infundibulum in these mice was similar to that in controls, suggesting that location of the infundibulum at the medial edge of the ovary at E17.5 does not rely on the presence of a continuous oviduct (Fig. 7C). These ovaries also appeared to have folded. This observation was consistent with our hypothesis that the infundibulum is tethered to the ovary through the CSL, and that this bond may be responsible for both ovary folding and relocation of the infundibulum. To test whether the CSL remained attached to the ovary and to this small fragment of infundibulum, we labelled the mesovarium and CSL of *Pax2*$^{del/del}$*; Pax8*$^{del/+}$ and *Pax2*$^{del/+}$*; Pax8*$^{del/del}$ samples using antibodies against aSMA and TNC (Fig. 7D). In both genotypes, the CSL was present, and the mesovarium appeared to become internalized on the dorsal side as the ovary folded, similarly to *Pax2*$^{del/+}$*; Pax8*$^{del/+}$ controls, in which a longer segment of oviduct was present (Fig. 7D - *top panels*). Importantly, the TNC+ CSL was present and appeared tethered to the medial edge of the ovary and to the persistent fragment of infundibulum in both *Pax2*$^{del/del}$*; Pax8*$^{del/+}$ and *Pax2*$^{del/+}$*; Pax8*$^{del/del}$ conditions (Fig. 7D - *bottom panels*). Overall, these data suggest that while the oviduct is required for ovary encapsulation, the infundibulum is sufficient to tether the ovary to the CSL.

Discussion

While the cortical/medullary structure of the mature ovary is well characterized, the mechanisms of organogenesis underlying the transition from the elongated structure of the early gonad had not been explained. The location of individual follicles within the cortex or medulla of the ovary appears to be crucial in determining their outcome (Cordeiro et al., 2015; Mork et al., 2012; Suzuki et al., 2015), but the

mechanisms that control regionalization of the ovary remain poorly understood. Using lightsheet and confocal imaging, we provide a robust image dataset that catalogs the complex events of ovary morphogenesis in the context of the extrinsic structures incorporated into the ovary and the other female reproductive structures that surround it. Importantly, the morphogenetic data presented here is an important first step towards integrating mechanical and architectural aspects of ovary development with the establishment of the medullary and cortical domains of the ovary, and the establishment of female fertility. In the present study, we propose a model of ovary morphogenesis that links the establishment of ovarian architecture and the functional regionalization of the ovary into cortical and medullary compartments with the morphogenesis of the oviduct and the CSL.

The dorsal face of the ovary is the center of action for most architectural changes during ovary morphogenesis. While the ovary initially develops on top of the mesonephros, the mesovarium progressively lines the dorsal aspect of the ovary. The CSL, which tethers the ovary to the dorsal body wall, originally appears on the medial ridge of the ovary, parallel to its longitudinal axis. Throughout ovary morphogenesis, the cranial region of the oviduct, the infundibulum, remains linked to the original anterior pole of the ovary through their mutual attachment to the CSL. Ovary folding is associated with relocation of the infundibulum to the medio-ventral opening of the ovarian hilum and incorporation of the CSL within the fold. The relocation of the oviduct and infundibulum is driven by the dorsal expansion of the mesovarium and the cranial expansion of the mesosalpinx, the region of the broad ligament that supports the oviduct (Harwalkar et al., 2021). This process leaves the ovary fully encapsulated, with the ovarian capsule arising from the growth and fusion of the mesovarium and the mesosalpinx (Agduhr, 1927). Using *Pax2* and *Pax8* deletion alleles as a functional model to investigate the role of the oviduct during ovary morphogenesis, we found that a continuous oviduct is required for ovary encapsulation. It will be interesting in the future to use this model to investigate whether the isolation of the ovary afforded by the capsule is significant for regionalization of the ovary into cortical and medullary compartments. We hypothesize that mechanical tension on the CSL drives the process of ovary folding. As the ovary folds toward its dorsal face, the mesovarium and associated vasculature and innervation, initially located on the medio-dorsal aspect of the ovary, become internalized inside the folded ovary, contributing new tissue to the initial gonad primordium. As the ovary folds, the OSE, located as a canopy on the ventral face of the ovary at E14.5, expands to the dorsal face. This process establishes the ovarian cortex and medulla. Oocytes and pre-granulosa cells that were originally in the dorsal region of the ovary become located in the medulla, in close proximity to newly internalized extrinsic components. This suggests that the allocation of follicles into medullary and cortical domains is driven by structural changes of the ovary during morphogenesis. It will be an exciting endeavor to integrate the morphogenetic events presented here with the dynamics of ovarian follicle formation to decipher the contribution of extrinsic molecular and mechanical signals to the establishment of the ovarian reserve.

We initially hypothesized that growth of the kidney induces tension on the CSL to drive ovary folding and relocation of the infundibulum. However, in *Pax2*$^{del/del}$*; Pax8*$^{del/+}$ and *Pax2*$^{del/+}$*; Pax8*$^{del/del}$ mice, which retain the CSL and lack kidneys, the ovary folded to varying degrees, suggesting that growth of the

kidney is not the sole driver of ovary folding. Our proposed model for ovary morphogenesis points to the CSL as the driver of the cascade of events that lead to the establishment of the architecture of the ovary. A previous study demonstrated that the gut mesentery, which is a fibromuscular connective tissue similar to the broad ligament and CSL, plays a crucial role in the establishment and maintenance of gut looping by exerting contractile forces on the developing intestine (Savin et al., 2011). One possibility is that the CSL displays autonomous contractility. It is also possible that several adjacent tissues contribute to ovary folding, including the kidney, CSL, infundibulum, and RO. Additional experiments will be necessary to tease apart the mechanical and molecular aspects of ovary folding. While the CSL originally develops in both males and females, it is maintained only in females to secure the ovary to the abdominal wall. In males, the CSL regresses to accommodate testis descent (Adham et al., 2002; Hutson et al., 1997; van der Schoot and Emmen, 1996). Although the testis does not normally undergo folding, it will be interesting in the future to determine whether some folding of the testis occurs in Persistent Mullerian Duct syndrome. In addition, while the testis is not permissive to the invasion of innervation (McKey et al., 2019; Svingen et al., 2012), the ovary integrates extrinsic components such as neurons and vasculature within the medulla, at least in part, as a result of folding over the growing mesovarium. The integration of these components likely influences the functional regionalization of the ovary.

This study also illuminates the developmental dynamics of the rete ovarii. We found that the CR remains at the interface between the ovary and mesonephric tissue throughout development, and corresponds to the dorsal protrusion of the ovarian domain. One hypothesis is that the CR and IOR act as a scaffold to tether the ovary to the mesonephros and allow integration of the mesovarium and other extrinsic components into the ovarian medulla as the ovary folds. In addition, the cells of the CR and/or IOR may produce guidance molecules that promote the invasion of extrinsic tissues into the ovary. The EOR develops inside the ovarian capsule in fetal life, but later resides in the periovarian fat pad in postnatal mice, leading to the hypothesis that the fetal ovarian capsule may give rise in postnatal life to both the ovarian bursa and the periovarian fat pad. While the absence of the EOR, and/or CR/IOR at E17.5 did not lead to overt differences in ovary folding, more experiments with these genetic models are required to investigate whether the loss of these regions affects folliculogenesis or the internal architecture of the ovary and exactly when during development loss of the RO occurs (Torres et al., 1995) . Importantly, while the RO is often dismissed as a vestigial remnant of the mesonephric tubules believed to degenerate in adulthood, we show that all three regions of the RO are maintained in the post-pubertal mouse ovary, and that the EOR remains a prominent structure that resides in the periovarian fat tissue. Together, these observations highlight the necessity of better understanding the biological function of the rete ovarii, and its role in female fertility.

Materials and methods

Mice. Unless otherwise stated, experiments were performed on wild-type CD-1 embryos, or mixed CD-1 and C57BL/6J embryos. The *Lgr5-Gfp-IRES-CreER* (*Lgr5-Gfp*; RRID: IMSR_JAX:008875) and Tg(*Nr5a1-eGFP*) (*Sf1-eGFP*) lines were previously described (Ng et al., 2014; Stallings et al., 2002) and maintained

on a C57BL/6 background. *Pax2* and *Pax8* ubiquitous deletion alleles (*Pax2*^{del} and *Pax8*^{del}) were obtained by crossing *Pax2*$^{f/f}$*; Pax8*$^{f/f}$ (Laszczyk et al., 2020) to *Wnt7a-Cre* (RRID: MMRRC_036637-JAX) (Winuthayanon et al., 2010), which we found to cause germline deletion in our animals. Offspring from this cross thus carried germline CRE-independent deletions of *Pax2* and *Pax8* and sired F2 offspring with ubiquitous deletion of *Pax2*, *Pax8*, or both. The *Pax2/8* flox mice were maintained on a mixed CD-1/C57BL/6J genetic background, and the *Wnt7a-Cre* mice were on a predominantly C57BL/6J genetic background. Primers used for PCR genotyping are listed in Supplementary Table 2. To collect embryos at specific developmental stages, males were set up in timed matings with several females. Females were checked daily for the presence of a vaginal plug. Date of the plug was considered embryonic day 0.5. All mice were housed in accordance with National Institutes of Health guidelines, in a barrier facility maintained at a temperature of 22 ± 0.1 °C, 30–70% humidity, within individually ventilated cages (Allentown; PNC75JU160SPCD3), and a controlled 12 h on / 12h off light cycle. All experiments were conducted with the approval of the Duke University Medical Center Institutional Animal Care and Use Committee (IACUC protocol # A089-20-04 9N).

Whole embryo collection and genotyping. Whole embryos at E14.5 were dissected in PBS-/-, fixed in 4% PFA/PBS overnight at 4ºC and gradually dehydrated using methanol dilutions for 45min each at room temperature: 25% MeOH/PBS; 50% MeOH/PBS; 75% MeOH/PBS; 100% MeOH. Embryos were then stored at -20ºC in 100% MeOH until required for staining. The amniotic sac of each embryo was used for sex genotyping: the tissue was incubated overnight at 55ºC in tissue lysis buffer with Proteinase K. The following day, genomic DNA was precipitated with isopropanol and purified by centrifugation. The pellet was resuspended in sterile dH2O and processed for PCR genotyping for *Sry* to determine the sex of the embryo. Primers used for PCR genotyping are listed in Supplementary Table 2.

Reproductive complex collection. Ovary/mesonephros/Müllerian duct complexes at desired stages were dissected in PBS-/-, with as little removal of surrounding tissue as possible to maintain the integrity of the complex. Samples were fixed for 30min at room temperature in 4%PFA/PBS. Following two 15min washes, samples were gradually dehydrated in MeOH dilutions (25% MeOH/PBS; 50% MeOH/PBS; 75% MeOH/PBS; 100% MeOH) for 15min each at room temperature. Samples were stored at -20ºC in 100% MeOH until required for staining.

iDISCO+ clearing and immunostaining for lightsheet imaging of whole embryos. When ready for analysis, E14.5 XX embryos were incubated overnight in, 66% dichloromethane (DCM), 33% methanol rocking at room temperature. Samples were treated with 5% H_2O_2 in methanol overnight at 4ºC. After washes in a reverse MeOH/PBS gradient (75% MeOH/PBS; 50% MeOH/PBS; 25% MeOH/PBS), rehydrated tissues were washed 15min in PBS 0.2% Triton X-102 (PTx.2), and permeabilized overnight at 37ºC in iDISCO permeabilization solution (PTx.2, 2.3% glycine, 20% DMSO). The following day, samples were transferred to iDISCO blocking solution (PTx.2 10% DMSO, 1.5% horse serum) for 6h at 37ºC.

Tissues were incubated in primary antibodies diluted in PTwH (PTx.2 with 0.001% heparin) 3% horse serum, 10% DMSO for 72h at 37 ºC. Samples were washed three times for 1h in PTwH and incubated for 48h in secondary antibodies diluted in PTwH 3% horse serum at 37ºC. After three 1h washes in PtWH, embryos were transferred to glass scintillation vials and progressively dehydrated into 100% methanol then incubated for 3h in 66% DCM, 33% methanol rocking at room temperature. Following two 30min washes in 100% DCM, samples were transferred into 100% dibenzylether (DBE) for final clearing. All primary antibodies and fluorophore-conjugated secondary antibodies used in this study are listed in Supplementary Tables 3 and 4 respectively.

Immunostaining for confocal imaging. Samples were gradually rehydrated into PBS through 10min washes in a reverse methanol gradient (75% MeOH/PBS; 50% MeOH/PBS; 25% MeOH/PBS), and transferred to PBS 0.1% Triton X-100 for 30min. Samples were then transferred to blocking solution (PBS; 1% Triton X-100; 10% horse serum) for 1h, and incubated overnight in primary antibodies diluted in blocking solution at 4ºC (Table S3). The next day, samples were washed three times for 30min in PBS 0.1% Triton X-100 and incubated overnight in secondary antibodies and Hoechst vital dye diluted 1:500 in blocking solution (Table S4). On day 3, samples were washed twice for 15min in PBS 0.1% Triton X-100 and transferred to PBS at 4ºC until ready to mount for confocal imaging (1h - 48h). Samples were mounted for imaging in polyvinyl alcohol mounting solution (stored at 4ºC) or DABCO mounting solution (stored at -20ºC) and stored until imaged. To image the dorsal and ventral sides of the same sample, we used 3D-printed reversible slides that can be flipped and imaged from both sides. The 3D model is available for download on the NIH 3D Print Exchange website at https://3dprint.nih.gov/discover/3DPX-009765. Angles of view for confocal microscopy are determined by the angle the tissue is mounted at, and thus may differ slightly from those chosen for 3D images captured with lightsheet microscopy.

iDISCO+CUBIC clearing and immunostaining for lightsheet imaging. Fetal reproductive complexes were immunostained and cleared with our combined iDISCO+CUBIC clearing method to allow imaging with the Zeiss Z.1 Lightsheet, which was only compatible with aqueous based clearing solutions (McKey et al., 2020, 2019). Briefly, isolated ovary/mesonephros samples went through the steps described above for iDISCO clearing. After incubation in DBE overnight, samples were transferred to 100% MeOH and progressively rehydrated to PBS through a reverse methanol gradient. Samples were then transferred into a 1:1 dilution of CUBIC Reagent-1 in dH2O (1/2Cubic R-1) for overnight incubation at 37ºC. The next day samples were transferred into 100% CUBIC R-1 for 24-48h. When sufficiently cleared, samples were washed in PBS and transferred to a 1:1 dilution of CUBIC Reagent-2 in PBS for 6h and 24-48h at 37ºC in 100% Cubic R-2 containing Hoechst nuclear dye. Once sufficiently cleared, samples were embedded in 2% agar/CUBIC R-2 in 1mL syringes and stored in the dark at RT until imaged.). Samples were imaged in CUBIC reagent-2 using the Z.1 Zeiss Lightsheet microscope (Carl Zeiss, Inc., Germany).

Image acquisition. We used confocal microscopy to image whole-mount immunostained gonads used for analysis of protein expression domains, and lightsheet microscopy when our goal was to generate 3D models of the developing embryo and/or ovary/mesonephros complexes. Images of the E14.5 iDISCO+-cleared whole embryo were acquired using a LaVision BioTec Ultramicroscope II lightsheet microscope (LaVision BioTec, GmbH, Germany) equipped with zoom body optics, an Andor Neo sCMOS camera, an Olympus MVPLAPO 2X/0.5 objective and a 5.7 mm working distance corrected dipping cap (total magnifications ranging from 1.3X to 12.6X with variable zoom). The whole embryo was mounted in a sample holder and submerged in a 100% DBE reservoir. The sample was imaged at 1.26X (0.63X zoom), using the three lightsheet configuration from both sides with the horizontal focus centered in the middle of the field of view, an NA of 0.026 (beam waist at horizontal focus = 28 µm), and a lightsheet width of 90%. Spacing of Z-slices was 10 µm. Confocal images of uncleared fetal ovary/mesonephros complexes were captured in the longitudinal plane on Zeiss LSM710 or LSM880 confocal microscopes and the affiliated Zen software (Carl Zeiss, Inc., Germany) using a 10X objective. Images of iDISCO+CUBIC-cleared isolated ovary/mesonephros complexes were acquired using a Zeiss Z.1 Lightsheet (Carl Zeiss, Inc., Germany). Lightsheet images were collected using the 5x NA 0.16 dry objective. Images were captured at 0.5 to 1X zoom, using the dual or single side lightsheet illumination (depending on size of sample), a lightsheet thickness of 2.5um, and a Z-interval of 1.2 to 2um. Image acquisition was performed with Zen software (Carl Zeiss, Inc., Germany).

Image processing. Confocal Z-Stacks were imported into FIJI software for minor processing, including cropping and rotations. All images of individual ovary/mesonephros complexes were oriented with the anterior end of the gonad to the left and posterior end to the right. Unless otherwise stated, all images presented in this study are maximum intensity projections of confocal Z-Stacks generated with FIJI. Final processing, such as channel overlays, brightness and contrast adjustments and figure compositions were made in Adobe Photoshop CC (Adobe, Inc., CA). Lightsheet Z-stacks were converted into .ims files using the Imaris file converter and imported into Imaris software for processing (Version 9.6; Bitplane, Inc., United Kingdom). Upon opening the file for the first time, x and y dimensions were downsampled to 50% of the original size (1920x1920x1.2px to 960x960x1.2px) for better file management. 3D volumes were rendered using the *maximum intensity* render mode, and isosurfaces were generated using the *surface creation wizard*, using an absolute threshold specified for each image and channel. To display specific regions and tissues, the *clipping plane* tool was applied. In cases where the antibodies labelled more than the region desired for display, the *cut surface* tool was used. Each channel was individually adjusted for brightness and contrast to capture still images of native data or 3D models using the *snapshot* tool (images captured as fixed size 1000 x 1000px transparent PNGs). Videos were captured using the *animation* tool in Imaris and edited using Adobe Premiere Pro CC software (Adobe, Inc., CA). All source images and 3D models will be made available upon request.

Acknowledgments

The authors would like to thank Benjamin Carlson and Lisa Cameron from the Duke Light Microscopy Core Facility for confocal and lightsheet imaging resources and assistance on lightsheet imaging and analysis. We are grateful to all members of the Capel laboratory for helpful discussions and suggestions on the work presented here, especially to Jordan Batchvarov for outstanding mouse care and technical support. We thank Dr. Vanda Lennon from the Mayo Clinic (Rochester, MN, USA) for the HuC/D antibodies, Dr. Harold Erickson (Duke University) for the TNC antibodies, and Greg Dressler for generating the Pax2 and Pax8 flox mice, and making them freely available to us through RB. This project was supported by a grant from the National Institutes of Health (Grant 1R01HD090050-0) (to B.C.) and R37HD30284 and Ben F. Love Chair to R.R.B. C.B. was supported by a grant from the National Institutes of Health (Grant R37HD039963). J.M. was supported by postdoctoral fellowships from the Fondation ARC pour la Recherche contre le Cancer (Award #SAE20151203560) and from the American Cancer Society (Award #130426-PF-17-209-01-TBG). A.E.O. was supported by a Diversity Supplement to HD30284. Lightsheet microscopy was supported by a grant from the National Institutes of Health (grant # 1S10OD020010-01A1) to the Duke Light Microscopy Core Facility and by a voucher from the Duke University School of Medicine.

Author contributions:

Conceptualization: JM, BC

Methodology: JM, DNA, CB, AEO

Formal Analysis: JM, DNA

Investigation: JM, DNA, CB, AEO

Visualization: JM, DNA, CB

Supervision: BC

Writing—original draft: JM, DNA, BC

Writing—review & editing: JM, DNA, CB, RRB, BC

Competing Interests

The authors declare no competing or financial interests.

References

Adham IM, Steding G, Thamm T, Büllesbach EE, Schwabe C, Paprotta I, Engel W. 2002. The Overexpression of the Insl3 in Female Mice Causes Descent of the Ovaries. *Mol Endocrinol* **16**:244–252. doi:10.1210/mend.16.2.0772

Agduhr E. 1927. Studies on the Structure and Development of the Bursa Ovarica and the Tuba Uterina in the Mouse. *Acta Zool* 8:1–133. doi:https://doi.org/10.1111/j.1463-6395.1927.tb00649.x

Archbald LF, Schultz RH, Fahning ML, Kurtz HJ, Zemjanis R. 1971. Rete ovarii in heifers: a preliminary study. *J Reprod Fertil* **26**:413–414. doi:10.1530/jrf.0.0260413

Bouchard M, Souabni A, Mandler M, Neubüser A, Busslinger M. 2002. Nephric lineage specification by

Pax2 and Pax8. *Genes Dev* **16**:2958–2970. doi:10.1101/gad.240102
Brachtendorf G, Kuhn A, Samulowitz U, Knorr R, Gustafsson E, Potocnik AJ, Fässler R, Vestweber D. Early expression of endomucin on endothelium of the mouse embryo and on putative hematopoietic clusters in the dorsal aorta. Dev Dyn. 2001 Nov;222(3):410-9. doi: 10.1002/dvdy.1199.
Brambell FWR. 1927. The Development and Morphology of the Gonads of the Mouse. Part II.--The Development of the Wolffian Body and Ducts. *Proc R Soc Lond Ser B Contain Pap Biol Character* **102**:206–221.
Brambell FWR, Hill JP. 1927. The development and morphology of the gonads of the mouse.— Part I. The morphogenesis of the indifferent gonad and of the ovary. *Proc R Soc Lond Ser B Contain Pap Biol Character* **101**:391–409. doi:10.1098/rspb.1927.0022
Bunce C, McKey J, Capel B. 2021. Concerted morphogenesis of genital ridges and nephric ducts in the mouse captured through whole-embryo imaging. *Development* **148**. doi:10.1242/dev.199208
Byskov AG. 1978. The Anatomy and Ultrastructure of the Rete System in the Fetal Mouse Ovary. *Biol Reprod* **19**:720–735. doi:10.1095/biolreprod19.4.720
Byskov AG, Lintern-Moore S. 1973. Follicle formation in the immature mouse ovary: the role of the rete ovarii. *J Anat* **116**:207–217.
Cordeiro MH, Kim S-Y, Ebbert K, Duncan FE, Ramalho-Santos J, Woodruff TK. 2015. Geography of follicle formation in the embryonic mouse ovary impacts activation pattern during the first wave of folliculogenesis. *Biol Reprod* **93**:88. doi:10.1095/biolreprod.115.131227
Duncan FE, Gerton JL. 2018. Mammalian oogenesis and female reproductive aging. *Aging* **10**:162–163. doi:10.18632/aging.101381
Fiorentino G, Garagna S, Zuccotti M. 2021. Three-dimensional imaging and reconstruction of the whole ovary and testis: a new frontier for the reproductive scientist. *Mol Hum Reprod*. doi:10.1093/molehr/gaab007
Ford MJ, Harwalkar K, Pacis AS, Maunsell H, Wang YC, Badescu D, Teng K, Yamanaka N, Bouchard M, Ragoussis J, Yamanaka Y. Oviduct epithelial cells constitute two developmentally distinct lineages that are spatially separated along the distal-proximal axis. *Cell Rep*. 2021 Sep 7;36(**10**):109677. doi: 10.1016/j.celrep.2021.109677.
Hadek R. 1958. Morphological and histochemical study on the ovary of the sheep. *Am J Vet Res* **19**:873–881.
Harikae K, Miura K, Kanai Y. 2013. Early gonadogenesis in mammals: Significance of long and narrow gonadal structure. *Dev Dyn* **242**:330–338. doi:10.1002/dvdy.23872
Harwalkar K, Ford MJ, Teng K, Yamanaka N, Yang B, Burtscher I, Lickert H, Yamanaka Y. 2021. Anatomical and cellular heterogeneity in the mouse oviduct—its potential roles in reproduction and preimplantation development†. *Biol Reprod*. doi:10.1093/biolre/ioab043
Huang C-C, Orvis GD, Kwan KM, Behringer RR. 2014. Lhx1 is required in Müllerian duct epithelium for uterine development. *Dev Biol* **389**:124–136. doi:10.1016/j.ydbio.2014.01.025
Hutson JM, Hasthorpe S, Heyns CF. 1997. Anatomical and Functional Aspects of Testicular Descent and Cryptorchidism*. *Endocr Rev* **18**:259–280. doi:10.1210/edrv.18.2.0298
Karl J, Capel B. 1998. Sertoli cells of the mouse testis originate from the coelomic epithelium. *Dev Biol* **203**:323–333. doi:10.1006/dbio.1998.9068
Kobayashi A, Behringer RR. 2003. Developmental genetics of the female reproductive tract in mammals. *Nat Rev Genet* 4:969–980. doi:10.1038/nrg1225
Kulibin AY, Malolina EA. 2020. Formation of the rete testis during mouse embryonic development. *Dev Dyn* **249**:1486–1499. doi:https://doi.org/10.1002/dvdy.242
Laronda MM, Unno K, Ishi K, Serna VA, Butler LM, Mills AA, Orvis GD, Behringer RR, Deng C, Sinha S, Kurita T. 2013. Diethylstilbestrol induces vaginal adenosis by disrupting SMAD/RUNX1-mediated cell fate decision in the Müllerian duct epithelium. *Dev Biol* **381**:5–16. doi:10.1016/j.ydbio.2013.06.024
Laszczyk AM, Higashi AY, Patel SR, Johnson CN, Soofi A, Abraham S, Dressler GR. 2020. Pax2 and Pax8 Proteins Regulate Urea Transporters and Aquaporins to Control Urine Concentration in the Adult Kidney. *J Am Soc Nephrol* **31**:1212–1225. doi:10.1681/ASN.2019090962
Lee S-H, Ichii O, Otsuka S, Elewa YHA, Yaser Hosney E, Namiki Y, Hashimoto Y, Kon Y. 2011. Ovarian cysts in MRL/MpJ mice are derived from the extraovarian rete: a developmental study. *J Anat* **219**:743–755. doi:10.1111/j.1469-7580.2011.01431.x

Lei L, Spradling AC. 2016. Mouse oocytes differentiate through organelle enrichment from sister cyst germ cells. *Science* **352**:95–99. doi:10.1126/science.aad2156

Lei L, Spradling AC. 2013. Mouse primordial germ cells produce cysts that partially fragment prior to meiosis. *Dev Camb Engl* **140**:2075–2081. doi:10.1242/dev.093864

Li L, Dong J, Yan L, Yong J, Liu X, Hu Y, Fan X, Wu X, Guo H, Wang X, Zhu X, Li R, Yan J, Wei Y, Zhao Y, Wang W, Ren Y, Yuan P, Yan Z, Hu B, Guo F, Wen L, Tang F, Qiao J. 2017. Single-Cell RNA-Seq Analysis Maps Development of Human Germline Cells and Gonadal Niche Interactions. *Cell Stem Cell* **20**:858-873.e4. doi:10.1016/j.stem.2017.03.007

Liu C, Peng J, Matzuk MM, Yao HH-C. 2015. Lineage Specification of Ovarian Theca Cells Requires Multi-Cellular Interactions via Oocyte and Granulosa Cells. *Nat Commun* 6:6934. doi:10.1038/ncomms7934

Liu C-F, Liu C, Yao HH-C. 2010. Building pathways for ovary organogenesis in the mouse embryo. *Curr Top Dev Biol* **90**:263–290. doi:10.1016/S0070-2153(10)90007-0

Martin E, Rodriguez-Martinez H, Dalin G, Castrillejo A. 1996. Development of the Genital Peritoneal Folds in Sheep. *Anat Histol Embryol* **25**:187–195. doi:https://doi.org/10.1111/j.1439-0264.1996.tb00081.x

Mayère C, Regard V, Perea-Gomez A, Bunce C, Neirijnck Y, Djari C, Bellido-Carreras N, Sararols P, Reeves R, Greenaway S, Simon M, Siggers P, Condrea D, Kühne F, Gantar I, Tang F, Stévant I, Batti L, Ghyselinck NB, Wilhelm D, Greenfield A, Capel B, Chaboissier MC, Nef S. Origin, specification and differentiation of a rare supporting-like lineage in the developing mouse gonad. *Sci Adv*. 2022 May 27;8(21):eabm0972. doi: 10.1126/sciadv.abm0972. Epub 2022 May 25.

McKey J, Bunce C, Batchvarov IS, Ornitz DM, Capel B. 2019. Neural crest-derived neurons invade the ovary but not the testis during mouse gonad development. *Proc Natl Acad Sci U S A* **116**:5570–5575. doi:10.1073/pnas.1814930116

McKey J, Cameron LA, Lewis D, Batchvarov IS, Capel B. 2020. Combined iDISCO and CUBIC tissue clearing and lightsheet microscopy for in toto analysis of the adult mouse ovary†. *Biol Reprod* **102**:1080–1089. doi:10.1093/biolre/ioaa012

Mork L, Maatouk DM, McMahon JA, Guo JJ, Zhang P, McMahon AP, Capel B. 2012. Temporal differences in granulosa cell specification in the ovary reflect distinct follicle fates in mice. *Biol Reprod* **86**:37. doi:10.1095/biolreprod.111.095208

Mossman HW, Duke KL. 1975. Comparative Morphology of the Mammalian Ovary, New edition. ed. Madison; London: University of Wisconsin Press.

Mullen RD, Behringer RR. 2014. Molecular genetics of Müllerian duct formation, regression and differentiation. *Sex Dev Genet Mol Biol Evol Endocrinol Embryol Pathol Sex Determ Differ* 8:281–296. doi:10.1159/000364935

Nef S, Stévant I, Greenfield A. 2019. Characterizing the bipotential mammalian gonad. *Curr Top Dev Biol* **134**:167–194. doi:10.1016/bs.ctdb.2019.01.002

Ng A, Tan S, Singh G, Rizk P, Swathi Y, Tan TZ, Huang RY-J, Leushacke M, Barker N. 2014. Lgr5 marks stem/progenitor cells in ovary and tubal epithelia. *Nat Cell Biol* **16**:745–757. doi:10.1038/ncb3000

Nicol B, Grimm SA, Chalmel F, Lecluze E, Pannetier M, Pailhoux E, Dupin-De-Beyssat E, Guiguen Y, Capel B, Yao HH-C. 2019. RUNX1 maintains the identity of the fetal ovary through an interplay with FOXL2. *Nat Commun* **10**. doi:10.1038/s41467-019-13060-1

Niu W, Spradling AC. 2020. Two distinct pathways of pregranulosa cell differentiation support follicle formation in the mouse ovary. *Proc Natl Acad Sci* **117**:20015–20026. doi:10.1073/pnas.2005570117

Orvis GD, Behringer RR. 2007. Cellular mechanisms of Müllerian duct formation in the mouse. *Dev Biol* **306**:493–504. doi:10.1016/j.ydbio.2007.03.027

Pepling M, Lei L. 2018. Germ Cell Nests and Germline Cysts In: Skinner MK, editor. Encyclopedia of Reproduction (Second Edition). Oxford: Academic Press. pp. 159–166. doi:10.1016/B978-0-12-801238-3.64710-4

Pepling ME. 2012. Follicular assembly: mechanisms of action. *Reproduction* **143**:139–149. doi:10.1530/REP-11-0299

Rastetter RH, Bernard P, Palmer JS, Chassot A-A, Chen H, Western PS, Ramsay RG, Chaboissier M-C, Wilhelm D. 2014. Marker genes identify three somatic cell types in the fetal mouse ovary. *Dev Biol* **394**:242–252. doi:10.1016/j.ydbio.2014.08.013

Renier N, Wu Z, Simon DJ, Yang J, Ariel P, Tessier-Lavigne M. 2014. iDISCO: a simple, rapid method to immunolabel large tissue samples for volume imaging. *Cell* **159**:896–910.

doi:10.1016/j.cell.2014.10.010
Roly ZY, Backhouse B, Cutting A, Tan TY, Sinclair AH, Ayers KL, Major AT, Smith CA. 2018. The cell biology and molecular genetics of Müllerian duct development. *WIREs Dev Biol* 7:e310. doi:https://doi.org/10.1002/wdev.310
Saito D, Tamura K, Takahashi Y. 2017. Early segregation of the adrenal cortex and gonad in chicken embryos. *Dev Growth Differ* **59**:593–602. doi:https://doi.org/10.1111/dgd.12389
Satoh M. 1985. The histogenesis of the gonad in rat embryos. *J Anat* **143**:17–37.
Savin T, Kurpios NA, Shyer AE, Florescu P, Liang H, Mahadevan L, Tabin CJ. 2011. On the growth and form of the gut. *Nature* **476**:57–62. doi:10.1038/nature10277
Stallings NR, Hanley NA, Majdic G, Zhao L, Bakke M, Parker KL. 2002. Development of a transgenic green fluorescent protein lineage marker for steroidogenic factor 1. *Mol Endocrinol Baltim Md* **16**:2360–2370. doi:10.1210/me.2002-0003
Soygur B, Jaszczak RG, Fries A, Nguyen DH, Malki S, Hu G, Demir N, Arora R, Laird DJ. Intercellular bridges coordinate the transition from pluripotency to meiosis in mouse fetal oocytes. *Sci Adv*. 2021 Apr 7;7(**15**):eabc6747. doi: 10.1126/sciadv.abc6747.
Soygur B, Laird DJ. Ovary Development: Insights From a Three-Dimensional Imaging Revolution. *Front Cell Dev Biol*. 2021 Jul 26;**9**:698315. doi: 10.3389/fcell.2021.698315.
Stévant I, Kühne F, Greenfield A, Chaboissier M-C, Dermitzakis ET, Nef S. 2019. Dissecting Cell Lineage Specification and Sex Fate Determination in Gonadal Somatic Cells Using Single-Cell Transcriptomics. *Cell Rep* **26**:3272-3283.e3. doi:10.1016/j.celrep.2019.02.069
Susaki EA, Tainaka K, Perrin D, Yukinaga H, Kuno A, Ueda HR. 2015. Advanced CUBIC protocols for whole-brain and whole-body clearing and imaging. *Nat Protoc* **10**:1709–1727. doi:10.1038/nprot.2015.085
Suzuki H, Kanai-Azuma M, Kanai Y. 2015. From Sex Determination to Initial Folliculogenesis in Mammalian Ovaries: Morphogenetic Waves along the Anteroposterior and Dorsoventral Axes. *Sex Dev Genet Mol Biol Evol Endocrinol Embryol Pathol Sex Determ Differ* 9:190–204. doi:10.1159/000440689
Svingen T, François M, Wilhelm D, Koopman P. 2012. Three-Dimensional Imaging of Prox1-EGFP Transgenic Mouse Gonads Reveals Divergent Modes of Lymphangiogenesis in the Testis and Ovary. *PLoS ONE* 7. doi:10.1371/journal.pone.0052620
Torres M, Gómez-Pardo E, Dressler GR, Gruss P. 1995. Pax-2 controls multiple steps of urogenital development. *Dev Camb Engl* **121**:4057–4065.
Upadhyay S, Zamboni L. 1982. Preliminary observations on the role of the mesonephros in the development of the adrenal cortex. *Anat Rec* **202**:105–111. doi:10.1002/ar.1092020112
van der Schoot P, Emmen J. 1996. Development, structure and function of the cranial suspensory ligaments of the mammalian gonads in a cross-species perspective; their possible role in effecting disturbed testicular descent. *Hum Reprod Update* 2:399–418. doi:10.1093/humupd/2.5.399
Wenzel JG, Odend'hal S. 1985. The mammalian rete ovarii: a literature review. *Cornell Vet* **75**:411–425.
Wilhelm D, Yang JX, Thomas P. 2013. Chapter Three - Mammalian Sex Determination and Gonad Development In: Thomas P, editor. Current Topics in Developmental Biology, Endocrine Gland Development and Disease. Academic Press. pp. 89–121. doi:10.1016/B978-0-12-416021-7.00003-1
Windley SP, Wilhelm D. 2015. Signaling Pathways Involved in Mammalian Sex Determination and Gonad Development. *Sex Dev Genet Mol Biol Evol Endocrinol Embryol Pathol Sex Determ Differ* 9:297–315. doi:10.1159/000444065
Winuthayanon W, Hewitt SC, Orvis GD, Behringer RR, Korach KS. 2010. Uterine epithelial estrogen receptor α is dispensable for proliferation but essential for complete biological and biochemical responses. *Proc Natl Acad Sci*. doi:10.1073/pnas.1013226107
Zhao F, Grimm SA, Yao HH-C. 2021. Molecular Actions Underlying Wolffian Duct Regression in Sexual Differentiation of Murine Reproductive Tracts. *Sex Dev* 1–9. doi:10.1159/000513878
Zhao F, Yao HH-C. 2019. A tale of two tracts: history, current advances, and future directions of research on sexual differentiation of reproductive tracts†. *Biol Reprod* **101**:602–616. doi:10.1093/biolre/ioz079
Zheng W, Zhang H, Gorre N, Risal S, Shen Y, Liu K. 2014. Two classes of ovarian primordial follicles exhibit distinct developmental dynamics and physiological functions. *Hum Mol Genet* **23**:920–928. doi:10.1093/hmg/ddt486